HHS Public Access

Author manuscript

Nat Aging. Author manuscript; available in PMC 2024 September 03.

Published in final edited form as:

Nat Aging. 2023 October ; 3(10): 1237–1250. doi:10.1038/s43587-023-00480-4.

The YAP–TEAD complex promotes senescent cell survival by lowering endoplasmic reticulum stress

Carlos Anerillas[1,✉], **Krystyna Mazan-Mamczarz**[1], **Allison B. Herman**[1], **Rachel Munk**[1], **Kwan-Wood Gabriel Lam**[1], **Miguel Calvo-Rubio**[2], **Amanda Garrido**[2], **Dimitrios Tsitsipatis**[1], **Jennifer L. Martindale**[1], **Gisela Altés**[1], **Martina Rossi**[1], **Yulan Piao**[1], **Jinshui Fan**[1], **Chang-Yi Cui**[1], **Supriyo De**[1], **Kotb Abdelmohsen**[1], **Rafael de Cabo**[2], **Myriam Gorospe**[1,✉]

[1]Laboratory of Genetics and Genomics, National Institute on Aging, National Institutes of Health, Baltimore, MD, USA.

[2]Translational Gerontology Branch, National Institute on Aging Intramural Research Program, National Institutes of Health, Baltimore, MD, USA.

Abstract

Sublethal cell damage can trigger senescence, a complex adaptive program characterized by growth arrest, resistance to apoptosis and a senescence-associated secretory phenotype (SASP). Here, a whole-genome CRISPR knockout screen revealed that proteins in the YAP–TEAD pathway influenced senescent cell viability. Accordingly, treating senescent cells with a drug that inhibited this pathway, verteporfin (VPF), selectively triggered apoptotic cell death largely by derepressing DDIT4, which in turn inhibited mTOR. Reducing mTOR function in senescent cells diminished endoplasmic reticulum (ER) biogenesis, triggering ER stress and apoptosis due to high demands on ER function by the SASP. Importantly, VPF treatment decreased the numbers of senescent cells in the organs of old mice and mice exhibiting doxorubicin-induced senescence. Moreover, VPF treatment reduced immune cell infiltration and pro-fibrotic transforming growth factor-β signaling in aging mouse lungs, improving tissue homeostasis. We present an alternative senolytic strategy that eliminates senescent cells by hindering ER activity required for SASP production.

✉**Correspondence and requests for materials** should be addressed to Carlos Anerillas or Myriam Gorospe., carlos.anerillasaljama@nih.gov; myriam-gorospe@nih.gov.

Author contributions

C.A. and K.M.-M. conceived and designed the study. S.D., K.A., R.d.C. and M.G. supervised the study. C.A., K.M.-M. and M.G. wrote the article. C.A., A.B.H., R.M., M.C.-R., A.G., D.T., J.L.M., G.A., M.R. and C.-Y.C. performed wet-lab and mouse experiments. K.M.-M., K.-W.G.L., Y.P., J.F. and S.D. performed bulk and single-cell sequencing and bioinformatic analyses. All authors reviewed and edited the article.

Competing interests

The authors declare no competing interests.

Additional information

Extended data is available for this paper at https://doi.org/10.1038/s43587-023-00480-4.

Supplementary information The online version contains supplementary material available at https://doi.org/10.1038/s43587-023-00480-4.

Cellular senescence is a dynamic state of cells responding to sublethal damage, characterized by persistent growth arrest and a secretory activity known as the SASP[1]. Other prominent traits of senescent cells include an altered metabolic profile, resistance to apoptosis, and enduring damage to DNA and other macromolecules. Although cellular senescence can be beneficial during processes like embryonic morphogenesis, tissue repair and cancer prevention, the aberrant accumulation of senescent cells is detrimental and leads to tissue decline and disease, as seen during the aging process[2].

Recently characterized compounds known as senolytics aim to reduce the accumulation of senescent cells within tissues[3]. Most of the known senolytics exploit the fact that senescent cells have endured severe damage but remain alive due to the implementation of robust antiapoptotic programs. Accordingly, many senolytics function by disrupting this balance in senescent cells, either by interfering with pro-survival signaling or by promoting the actions from pro-apoptotic factors[4,5].

To identify alternative strategies for removing senescent cells, we performed a whole-genome CRISPR screen to identify genes that function to preserve the viability of senescent cells. We report the discovery of several genes encoding proteins in the Hippo pathway, which modulates the transcriptional activity of the YAP–TEAD complex, as being essential for maintaining senescent cell survival. Moreover, we found that treatment with a drug named VPF, which inhibits the interaction between YAP and TEAD and thus prevents the transcriptional function of this complex, caused senolysis in several cell culture models of senescence. Treatment of senescent cells with VPF triggered ER stress and subsequent apoptosis. Detailed characterization of VPF actions revealed that, in senescent cells, YAP–TEAD repressed the transcription of DDIT4, an inhibitor of mTOR[6]; accordingly, treatment with VPF reduced mTOR function and lowered the biosynthesis of the ER membrane. We propose a model whereby interfering with the YAP–TEAD–DDIT4–mTOR pathway renders senescent cells more susceptible to senolysis due to their unique requirement for robust protein synthesis to sustain the SASP. In support of this model, ablating the SASP by silencing RELA rescued senescent cells from the apoptotic impact of inhibiting YAP–TEAD or mTOR. Finally, VPF treatment reduced the burden of senescent cells in live organisms, as seen in naturally aged mice and mice exhibiting doxorubicin-induced senescence, and improved tissue homeostasis. Considering these findings, we propose that metabolic targeting of the secretory machinery can sensitize senescent cells to achieve senolysis.

Results

CRISPR screen reveals YAP–TEAD promotes senescence viability

A CRISPR screen was devised to identify pathways that sensitize senescent cells to senolysis. Briefly, we triggered etoposide-induced senescence (ETIS) in WI-38 human diploid fibroblasts by treatment with 50 μM etoposide following the scheme indicated (Fig. 1a,b). After confirming the presence of senescent cells by assessing senescence-associated β-galactosidase (SA-β-gal) activity and 5-bromo-2′-deoxyuridine (BrdU) incorporation (Fig. 1c–e), we transduced ETIS WI-38 cells with a human, whole-genome CRISPR knockout library (Brunello)[7] at a multiplicity of infection (MOI) of 0.44 after optimization

(Extended Data Fig. 1a). Seventy-two hours later, we collected a reference sample ($t = 0$), and incubated cells for an additional 14 d before analysis to ensure the identification of guide RNAs (gRNAs) with slow kinetics. To identify genes relevant for viability, we focused on gRNAs showing decreased representation after 14 d (Fig. 1f and Supplementary Tables 1 and 2). Enrichr analysis revealed that the Hippo–MST1 pathway, including the YAP–TEAD complex, was present at the top of multiple ranks such as Gene Ontology (GO) Biological Process, Reactome or GO Cellular Component (Fig. 1g,h). We validated these results by individually silencing those genes in the Hippo YAP–TEAD pathway that were reduced in the CRISPR screen (*YAP1*, *TEAD2*, *MOB1A*, *MAP4K1* and *TAOK2*). Among them, silencing *TEAD2*, *MOB1A* and *MAP4K1* mRNAs reduced the number of viable senescent cells (Extended Data Fig. 1b,c). Western blot analysis revealed that the levels of Hippo components were unchanged (Extended Data Fig. 1d), but the activity of the YAP–TEAD complex increased in senescent cells, as a heterologous luciferase reporter driven by a TEAD-responsive promoter and the levels of YAP–TEAD transcriptional targets *ANKRD1* and *TGFB2* mRNAs[8–11] increased in senescent cells (Fig. 1i,j). Silencing YAP1 or TEAD2 reduced the levels of *ANKRD1* and *TGFB2* mRNAs back to control levels, while the levels of *CDKN2A (p16)* mRNA, encoding a senescence marker[12], remained elevated (Fig. 1j).

We then tested in senescent and proliferating WI-38 cells the impact of the drug VPF, which functions by disrupting the interaction between YAP and TEAD[13]. As shown in Fig. 1k, after incubation with increasing concentrations of VPF for 72 h, senescent WI-38 fibroblasts were significantly more sensitive to VPF than proliferating fibroblasts. We extended this analysis to other models of senescence, including WI-38 fibroblasts undergoing replicative senescence (RS) or rendered senescent following exposure to ionizing radiation (ionizing radiation-induced senescence (IRIS); Methods); senescence was confirmed by assessing SA-β-gal activity and BrdU incorporation (Extended Data Fig. 1e,f). VPF treatment selectively reduced the viability of senescent cells (Fig. 1k,l) and elevated caspase-3/caspase-7 activity[14,15] (Fig. 1m and Extended Data Fig. 1g). To confirm that VPF triggered cell death in senescent cells through apoptosis, cell death was rescued by blocking caspase-3/caspase-7 activity with the pan-caspase inhibitor Z-VAD-FMK (Fig. 1n,o). Similarly, VPF triggered senolysis in other human cell types (diploid fibroblasts BJ and IMR-90, human small airway epithelial cells (HSAECs) and human umbilical vein endothelial cells (HUVECs)) rendered senescent by treatment with etoposide (Extended Data Fig. 1e,f,h,i). Finally, recently reported inhibitors of YAP–TEAD function CA3, MYF-01-37 and K-975 also triggered death of senescent WI-38 cells (Fig. 1p). Together, these data suggest that senescent cells can be selectively eliminated by inhibiting YAP–TEAD function.

Inhibiting YAP–TEAD induces apoptosis and endoplasmic reticulum stress

To investigate how the inhibition of YAP–TEAD by VPF triggered apoptosis in senescent cells, we studied the effects of VPF at 48 h, when signs of cell death began, to understand the signaling changes leading to apoptosis. First, we confirmed that VPF reduced the interaction between YAP and TEAD and hence YAP–TEAD function in this paradigm. As shown in Fig. 2a, VPF treatment reduced YAP–TEAD luciferase activity and hindered the interaction of YAP and TEAD, as observed by co-immunoprecipitation (co-IP) analysis

(TEAD IP) followed by western blot analysis to detect YAP levels in the IP (Extended Data Fig. 2a,b).

We then performed RNA-sequencing (RNA-seq) analysis of untreated and VPF-treated senescent cells (ETIS) and used gene set enrichment analysis (GSEA) to identify differences in the two transcriptomes (GSE221254). Initial analysis confirmed the inhibition of YAP–TEAD, as determined by the reduced levels of transcriptional YAP–TEAD targets *ANKRD1*, *TGFB2*, *WNT5B*, *LATS2*, *NF2*, *ADAMTS1* and *AMOTL1* mRNAs and GSEA association with YAP targets upon VPF treatment (Extended Data Fig. 2c,d)[16,17]. As shown in Fig. 2b, most of the top-ranked GSEA gene sets associated with VPF treatment were related to the ER stress response, including the unfolded protein response (UPR) and the integrated stress response (ISR), both of which converge on the central effector eIF2α (EIF2A)[18]. Moreover, the additional YAP–TEAD inhibitors similarly reduced the levels of *ANKRD1* and *TGFB2* mRNAs, transcriptionally regulated by YAP–TEAD (Extended Data Fig. 2e) and increased the levels of representative ER stress response transcripts (*DDIT4*, *DDIT3*, *ASNS* and *PSAT1* mRNAs; Fig. 2c and Extended Data Fig. 2f). The latter effect was also observed when silencing TEAD2 in ETIS WI-38 cells (Extended Data Fig. 2g). Additionally, and in line with recent reports[11], we found that the epithelial–mesenchymal transition (EMT) signature in senescent cells was reduced by VPF treatment (Extended Data Fig. 2h). Nonetheless, we focused on ER stress given its predominant representation in pathway analysis and its strong link to apoptosis[19], as supported by the increased levels of mRNAs encoding pro-apoptotic proteins like PUMA, PMAIP1, TNFRSF10B and BID[4,20] upon VPF treatment (Fig. 2c). These observations were validated by reverse transcription followed by quantitative PCR (RT–qPCR) analysis in both VPF-treated and TEAD2-silenced senescent WI-38 cells (Fig. 2d,e). Similar increases in these pro-apoptotic transcripts were observed in ETIS WI-38 cells treated with additional YAP–TEAD inhibitors (Extended Data Fig. 2i), further supporting the notion that the pro-apoptotic effects caused by VPF treatment are specifically linked to YAP–TEAD inhibition.

To further characterize the mediators of VPF-induced ER stress in senescent cells, we focused on the ER stress response factors EIF2A and ATF4, as these proteins are shared effectors of the ISR and the UPR[19]. As shown, the levels of phosphorylated (p-) EIF2A and ATF4 increased in VPF-treated senescent cells (Fig. 2f), but the levels of XBP1s and ATF6 (Extended Data Fig. 2j), which are key effectors of alternative ER stress responses[21], did not. GSEA analysis also pointed to PERK (EIF2AK3), an upstream activator of EIF2A previously related to senescence[22], as a prominent contributor to the transcriptomic signature displayed by VPF-treated senescent cells (Extended Data Fig. 2k). In fact, PERK silencing reduced both EIF2A phosphorylation and cell death (Extended Data Fig. 2l–n) caused by VPF treatment in senescent cells. Moreover, in a model of systemic senescence triggered by a single injection of doxorubicin (10 mg per kg body weight), VPF treatment (four daily treatments from day 6 onward) caused ER stress in p21-positive cells found in lungs from mice analyzed at day 10 after doxorubicin injection (Fig. 2g)[20,23]. Comparison between VPF-treated and untreated senescent (ETIS) WI-38 fibroblasts using transmission electron microscopy (TEM) showed that the rough ER of VPF-treated cells appeared more swollen and less organized (Fig. 2h and Extended Data Fig. 2o,p), two signs of ER stress commonly

assessed using this technique[24,25]. Together, these data suggest that VPF treatment promotes apoptosis by signaling through the ER stress response factors PERK, EIF2A and ATF4.

Since the YAP–TEAD complex can both enhance and repress transcription[16,17,26], we examined the top 10 mRNAs that increased or decreased with VPF treatment and focused on known direct targets of YAP–TEAD, such as *DDIT4*, *DDIT3*, *ASNS*, *DUSP1*, *PSAT1*, *SLC6A9*, *PCK2*, *OXTR* and *COL11A1* mRNAs (Fig. 2i). We then assessed the kinetics of expression of each mRNA, including *ANKRD1* mRNA as a control readout of YAP–TEAD function, following the addition of VPF (Fig. 2j). We observed that only *DDIT4*, *OXTR* and *COL11A1* mRNAs, along with the control, *ANKRD1* mRNA, changed significantly by 8 h (Fig. 2j). Interestingly, *DDIT4* mRNA, which is transcriptionally repressed by YAP–TEAD[26], is part of the ER stress response transcriptomic program[18] (Fig. 2c) and appeared to increase before other ER stress-related transcripts (*DDIT3*, *ASNS* and *PSAT1* mRNAs; Extended Data Fig. 2q). Because the levels of ATF4 (and p-EIF2A) increased by 48 h of VPF treatment (Fig. 2k), when *DDIT3*, *ASNS* and *PSAT1* mRNAs were strongly elevated (Fig. 2j), the derepression of *DDIT4* mRNA might represent an earlier event that later leads to a full ER stress response. Chromatin immunoprecipitation (ChIP) analysis indicated that VPF treatment reduced the association of YAP to a binding region in the *DDIT4* gene promoter[26] (Extended Data Fig. 2r). These findings support the hypothesis that *DDIT4* mRNA derepression is a direct consequence of YAP–TEAD inhibition rather than an indirect result of the ER stress response.

As p53 increases *DDIT4* mRNA levels transcriptionally[27], we hypothesized that *DDIT4* mRNA derepression could be mitigated by silencing p53 in VPF-treated senescent cells. Interestingly, as shown in Extended Data Fig. 2s, *DDIT4* mRNA levels were lower in senescent cells compared to proliferating cells, even though p53 activity is elevated in senescence, but p53 silencing reduced the levels of *DDIT4* mRNA that had been elevated by VPF treatment. These data suggest that YAP–TEAD function could counteract some pro-apoptotic features of p53 in senescent cells, as observed for *DDIT4* mRNA. Finally, to confirm that DDIT4 contributes to ER stress and subsequent senolysis in VPF-treated senescent cells, we silenced DDIT4 before treatment with VPF. Reducing DDIT4 levels decreased both p-EIF2A levels and apoptotic cell death caused by VPF (Fig. 2l–n). Accordingly, the VPF-mediated rise in mRNAs related to the ER stress response and apoptosis was diminished after silencing DDIT4 (Fig. 2o,p). In sum, ER stress and senolysis caused by VPF appear to be mediated by DDIT4 derepression.

Inhibiting endoplasmic reticulum biogenesis by DDIT4 induces senolysis

Given that DDIT4 inhibits mTOR[6,28], we analyzed if VPF treatment affected signaling through PI3K–AKT–mTOR in senescent cells. In agreement with the known function of DDIT4 as an inhibitor of RHEB[6,29], we found that mTOR and S6K phosphorylation were reduced by VPF treatment, leaving AKT unaffected (Fig. 3a). Moreover, VPF treatment inhibited mTOR after only 8 h (Fig. 3b), coinciding with the derepression of *DDIT4* mRNA (Fig. 2j) and before the full implementation of ER stress-related increase in the levels of p-EIF2A and ATF4 (Fig. 2k). Silencing DDIT4 significantly mitigated the inhibition of S6K phosphorylation caused by VPF (Fig. 3c), suggesting that DDIT4 also suppresses mTOR

in this system. In sum, mTOR inhibition by DDIT4 preceded ER stress in senescent cells treated with VPF.

These observations prompted us to test if mTOR inhibition could cause ER stress in senescent cells. First, we tested the mTOR inhibitor Torin1, previously used in senescent cells[30,31], but we used the higher dose of 100 nM, which did not reduce the viability of proliferating cells but caused significant death in senescent cells (Extended Data Fig. 3a,b), as reported[32]. As shown, Torin1 treatment caused a marked increase in p-EIF2A in senescent cells, along with decreased p-S6K (Fig. 3d); as seen in VPF-treated cells, this was the only branch of the ER stress response triggered by Torin1, as the levels of ATF6 and XBP1s were not increased by mTOR inhibition (Extended Data Fig. 3c). Moreover, Torin1 treatment also elevated the levels of mRNAs encoding pro-apoptotic proteins that were increased by VPF treatment (Extended Data Fig. 3d). Together, these findings support the notion that DDIT4 inhibition of mTOR is largely responsible for VPF-caused ER stress. In fact, simultaneous treatment with Torin1 and VPF neither augmented senolysis (Extended Data Fig. 3e) nor increased the levels of ER stress-related *DDIT3*, *ASNS* and *PSAT1* mRNAs (Extended Data Fig. 3f) when compared to VPF treatment alone, possibly indicating that DDIT4-dependent mTOR inhibition cannot be further potentiated by adding direct mTOR inhibitors such as Torin1. In agreement with our hypothesis, direct mTOR inhibition did not increase *DDIT4* mRNA levels (Extended Data Fig. 3f), suggesting that the rise observed for this mRNA upon VPF treatment is a direct consequence of its derepression and not just part of a transcriptomic ER stress response.

We sought a deeper understanding of how mTOR inhibition caused ER stress in senescent cells. YAP and TEAD support the ER enlargement required in cells with high demand for protein production[33] and mTOR is required for ER biogenesis[34,35]. Therefore, we wondered whether mTOR inhibition caused by VPF might trigger ER stress by reducing the size of the ER. mTOR controls ER biogenesis at least in part by increasing the expression of two key enzymes in the production of phosphatidylcholine (PtdCho), lipin-1 (LPIN1) and CCTα (PCYT1A)[36–38] (Fig. 3e). Importantly, treatment with VPF or Torin1 decreased lipin-1 and CCTα levels in senescent cells (Fig. 3f). To measure the relative size of the ER for each condition, we used a commercial ER tracker (Methods) to quantify the relative areas positive for the tracker dye in multiple cells from the different treatments; as shown, treatment with VPF or Torin1 significantly reduced the red area, a surrogate measure of ER size (Fig. 3g and Extended Data Fig. 3g). Both treatments also reduced the levels of PtdCho per cell (Fig. 3h), suggesting that these drugs might lower the production of PtdCho, which is necessary for ER biogenesis. In further support of this hypothesis, we observed that the reduction in ER triggered by treatment with VPF or Torin1 was partially rescued by PtdCho supplementation (Fig. 3i and Extended Data Fig. 3h). Moreover, both p-EIF2A and cell death caused by VPF or Torin1 were mitigated by PtdCho supplementation (Fig. 3j,k). These observations support the notion that active YAP–TEAD preserves mTOR function, in turn enhancing ER biogenesis and avoiding ER stress and apoptosis.

mTOR function was proposed to support the SASP[30,31] and mTOR inhibition is widely accepted as a senomorphic intervention[39]. Therefore, we tested whether mTOR inhibition by VPF or Torin1 reduced the SASP, as well as the impact of the reduced SASP load on

ER stress. Strikingly, neither treatment (VPF or Torin1) reduced the levels of SASP mRNAs (Extended Data Fig. 3i) or the presence of SASP factors in conditioned media (Extended Data Fig. 3j). These observations could be explained by the higher doses of Torin1 used in our study (four times higher doses than those used previously[30,31]), or because our treatment regimens were much shorter (2 d instead of 6 d)[30,31]. In other words, a stronger and more acute mTOR inhibition could have a more severe impact on ER biogenesis rather than affecting the SASP.

Accordingly, we tested whether the production of SASP factors contributed to making senescent cells more sensitive than proliferating cells to ER size reduction by VPF or Torin1. First, we performed single-cell (sc)RNA-seq transcriptomic analysis of senescent (ETIS) WI-38 cells treated with VPF for 72 h, the time in which the most sensitive cells from the population had been eliminated by apoptosis, to evaluate whether the highest SASP-secreting cells were also the most vulnerable (Fig. 3l). We also sequenced untreated ETIS WI-38, integrated both datasets and clustered them for comparison (Fig. 3m). When we evaluated the expression of 132 SASP-related mRNAs for each of the defined clusters, we observed that, in most cases, after VPF selection, there was a marked reduction in both the expression levels (1.1- to 4.2-fold decrease) and the percentages of cells expressing these transcripts (8–30.7% decrease; Fig. 3n). These observations indicate that, after VPF treatment for 72 h, the remaining cells displayed a much lower secretory phenotype in all the clusters, which was validated by bulk RT–qPCR analysis (Fig. 3o). As anticipated, the same VPF treatment elevated the expression of ER stress response markers in most of the clusters as well (GSE221254). Additionally, the senescent cells in the control group expressing the highest levels of SASP factors greatly overlapped with those displaying a high expression of ER stress-related transcripts, even without VPF treatment (Extended Data Fig. 3k). Such overlap seemed specific, as other gene sets like ‘oxidative phosphorylation’ displayed a rather different pattern, and further suggested that cells with a robust SASP program could be primed to die by additional ER stress potentiation upon VPF treatment. In sum, senescent cells with high SASP expression levels appear more sensitive to VPF-triggered senolysis.

Second, to validate whether the sensitivity to VPF treatment was truly dependent on the SASP, we lowered nuclear factor (NF)-κB activity by silencing RELA[40,41] and evaluated the effect of VPF treatment on ER stress and senolysis. In keeping with earlier findings that NF-κB repression decreased ER stress markers in senescence[42], p-EIF2A levels were reduced after RELA silencing in senescent cells (Fig. 3p). Importantly, silencing RELA diminished p-EIF2A triggered by treatment of senescent cells with VPF or Torin1 (Fig. 3p and Extended Data Fig. 3l), and also mitigated cell death and caspase-3/caspase-7 activity (Fig. 3q,r and Extended Data Fig. 3m). As expected, silencing RELA reduced the levels of mRNAs encoding prominent SASP factors like interleukin (IL)1A, IL6 or IL8 (Extended Data Fig. 3n), and lowered the levels of key SASP factors in conditioned media (Extended Data Fig. 3o). In sum, these findings suggest that senescent cells are more sensitive to VPF (and possibly other ER-targeting drugs) because they actively produce SASP factors. We propose that senescent cells cope with SASP-triggered ER stress by activating YAP–TEAD, which in turn represses DDIT4, an essential step to retain mTOR function and preserve a robust ER biogenesis. Disruption of this delicate balance by inhibiting YAP–TEAD (using VPF) leads to excessive ER stress and subsequent apoptosis (Fig. 3s).

VPF treatment reduces senescent cell burden in mice

In light of our findings using VPF in cultured cells, we evaluated whether VPF treatment might also cause senolysis in mouse models of senescence such as natural aging or doxorubicin-induced senescence[4,14,23]. To study if VPF might influence the burden of senescent cells in naturally aged tissues, mice were treated with VPF monthly, starting at 22 months old until they reached 24 months of age; in parallel, mice received either vehicle (dimethylsulfoxide (DMSO)) or the known senolytic ABT-737 following published regimens[43]. One week after the last round of treatments, kidney, liver and lung tissue were collected (Fig. 4a). Importantly, we observed a substantial decrease in the presence of the senescence markers p16 and p21 by immunofluorescence analysis (Fig. 4b,c and Extended Data Fig. 4a,b) and *p16* and *p21* mRNAs by RT–qPCR analysis (Fig. 4d and Extended Data Fig. 4c) in the tissues from old mice treated with VPF or ABT-737 compared to old DMSO-treated animals. These observations were reproduced in mice injected with doxorubicin (or DMSO) to trigger senescence systemically. Such mice were then treated with VPF once daily for the final 4 d (Extended Data Fig. 4d), and samples were collected on day 10 from the start of doxorubicin treatment. The levels of senescence were reduced in the lung, kidney and liver of these mice, as determined by quantifying both *p21* mRNA levels and p21-positive cells (Extended Data Fig. 4e–g), as well as serum GDF15 levels, which also declined in naturally aged mice treated with senolytics (Extended Data Fig. 4h).

Analysis of physiological parameters following these treatments revealed that old mice treated with VPF or ABT-737 appeared healthier overall compared to DMSO-treated mice (Fig. 4e), as judged, for instance, by the incidence of alopecia in the different groups (Fig. 4f and Extended Data Fig. 5a). scRNA-seq analysis was then used to assess the lung, as our initial screen was performed in lung fibroblasts and the lung is often used to evaluate cell senescence[5,14,44]. We used a total of 16 mice (4 mice per group), but analyzed a total of 8 samples (2 mice per group), as pairs of mouse lungs from the same experimental group were combined. scRNA-seq analysis identified 28 different clusters corresponding to different cell types (Fig. 4g and Extended Data Fig. 5b), including most of the known lung cell lineages[45,46]. Although *Cdkn2a* mRNA is modestly detected by scRNA-seq analysis[46], both VPF and ABT-737 reduced its expression levels in arterial endothelial cells, type 1 fibroblasts, and type 1 and 2 capillary aerocytes (Extended Data Fig. 5c). Given the lack of definitive markers of cell senescence markers in vivo, we analyzed prominent senescence-associated transcriptomic signatures (p53, transforming growth factor (TGF)-β, inflammatory SASP) per cluster by comparing ‘old DMSO’ to the rest of the groups together, as clusters in which senescence-associated transcriptomes were elevated and reduced by the two senolytics might be considered to be senescent. This analysis revealed that the most consistently senescence-associated and senolytic-responsive cell types included type 1 fibroblasts and type 1 capillary aerocytes, along with ciliated cells in this case (Fig. 4h and Supplementary Table 4). Other clusters in which one or two senescence transcriptomic signatures increased with age and declined with senolytics (for example, inflammatory SASP and/or p53 and TGF-β transcriptomic signatures) were type 1 pneumocytes, type 2 capillary aerocytes and basal cells (Fig. 4h and Supplementary Table 4). The incomplete effects of age and senolytics for some clusters might be explained by factors such as the absence of some senescence-associated transcriptomic signatures in some

cell types with aging, possible secondary senescence caused by neighboring cells, or the imperfect parameters with which senescent cells are defined.

From the analysis of cell type percentages per sample (Supplementary Table 5), one particular cell lineage stood out, lymphocytes. Immune infiltration within the lung is a hallmark of the aging lung[47,48], translating into a significant increase in the proportion of lymphocytes with age, which was markedly reduced with VPF treatment and moderately with ABT-737 (Fig. 4i). These observations were supported by flow cytometry assessment of immune cells in lung ($CD45^+$, a broad marker of immune cells; Extended Data Fig. 5d). Specifically, treatment with senolytics (especially VPF) reduced the proportion of $CD8^+$T cells, B cells and natural killer (NK) cells in old mice. Given that one of the senescent-like cell types in our study, the type 1 capillary aerocytes, critically controls immune trafficking within the lung[49], its pro-inflammatory phenotype in aging (Extended Data Fig. 5e) likely contributes to immune attraction to the lung. Importantly, treatment with senolytics also decreased $CD8^+$T cell and B cell activation[50], as shown by GSEA (Extended Data Fig. 5f), indicating that these cells decline in number and are also less active. Importantly, $CD8^+$T cells, NK cells and even B cells have been proposed as main contributors to the clearance of senescent cells within organs[51–54]. Therefore, a decrease in the number of senescent cells could naturally reduce immune infiltration and activation.

Another sign of the aging lung is the establishment of a fibrotic environment, often linked to decreased organ function[47,55]. Moreover, the presence of senescent cells in several organs exacerbates fibrosis[44,56,57], which can be improved with senolytics. Here, we observed that both senolytics included in our study reduced pro-fibrotic TGF-β signaling arising from type 1 fibroblasts and type 1 capillary aerocytes (Fig. 4h,j,k). This change translates into mitigated pro-EMT signaling, as observed in key lung neighboring cell types such as type 1 pneumocytes, basal cells, ciliated cells, type 2 capillary aerocytes and arteriolar endothelial cells (Fig. 4j,l). Evaluation of collagen deposition, a sign of tissue fibrosis, by staining the different experimental groups with Masson's trichrome (MTC) showed that the rise in MTC staining with aging was diminished by VPF or ABT-737 treatment in the lung (Fig. 4m,n), as well as in liver and kidney (Extended Data Fig. 5g,h). In turn, serum markers related to the function of these organs, such as blood urea nitrogen for the kidney and aspartate transaminase for the liver[4,14], returned to levels closer to normal with either treatment (Extended Data Fig. 5i,j). In sum, VPF and ABT-737 partially restored lung homeostasis by reducing TGF-β-related pro-fibrotic signaling, which hinders the normal function of different tissues in aging[48,58,59]. The same is likely true for liver and kidney, as we also observed substantially less fibrosis in these and improved function by serum analysis.

In conclusion, the results presented here support the notion that VPF treatment is a promising strategy to reduce the burden of senescent cells in detrimental scenarios such as aging or chemotherapy-induced senescence. Reduced pro-fibrotic and pro-inflammatory signaling, as we observed in the lung, likely contributes to the reduction in age-related fibrosis and the improvement in organ homeostasis.

Discussion

This study uncovers a vulnerability of senescent cells linked to a unique metabolic feature, namely the robust secretion of SASP factors. As suggested previously[42], the ER of senescent cells is subject to stress due to high demands of protein synthesis required to implement the SASP[60,61]. Our results show that reducing ER biosynthesis by inhibiting production of PtdCho causes a metabolic crisis that primes senescent cells to die by apoptosis. Although VPF treatment was previously found to cause ER stress[62], here we have connected the derepression of DDIT4 by YAP–TEAD inhibition to the reduced mTOR function and subsequent impairment of ER biogenesis.

Senescent cells are believed to reprogram their metabolism to cope with their heightened secretory needs[63]. Organelles such as the ER, the Golgi and lysosomes appear to require efficient coordination to support the SASP[64]. Current evidence suggests that mTOR is needed to support the SASP early in senescence[30,31]; therefore, inhibiting mTOR was proposed as a strategy to reduce SASP factor release by senescent cells[39]. However, we found that higher doses of mTOR inhibitors led to senolysis, as reported[32], while further mTOR inhibition did not lower SASP factor secretion, but instead decreased ER biogenesis associated with a reduction in the levels of lipin-1 and CCTα, two key enzymes in PtdCho biogenesis[36–38].

The apoptotic cell death triggered by the VPF inhibition of YAP–TEAD in senescent cells suggests that YAP–TEAD functions as a pro-survival pathway in senescence, recapitulating the pro-survival effects of this pathway in other cell responses[65]. Even though VPF had a more robust effect, other YAP–TEAD inhibitors (CA3, MYF-01-37 and K-975) also reduced the viability of senescent cells in culture, possibly expanding the interventions that could be exploited in vivo. Their limited senolytic impact could be linked to a selective inhibition of specific TEAD proteins (TEAD1–TEAD4), and this could be a desirable feature for some cell types. It is also possible that a senolytic action could be delayed due to variations in the pharmacodynamics of each drug. All these unknown features remain to be addressed in future experiments.

Interestingly, an EMT-like phenotype crucial for implementing senescence over apoptosis[20] seems to be suppressed by VPF treatment (Extended Data Fig. 2c), as we and others have found[11]. Thus, VPF might promote apoptosis not only by triggering ER stress, but also by suppressing an EMT program. We must also consider the alternative functions that YAP may acquire after the YAP–TEAD interaction is disrupted. For example, the interaction of YAP with proteins like p63 or p73 (ref. 66,67) could be linked to the pro-apoptotic role of YAP, and the prevention of aging in stromal cells by YAP/TAZ[68]. This notion could also help explain earlier findings that silencing Hippo's upstream regulators MOB1A and MAP4K1 promotes cell death; perhaps their role is to prevent YAP's pro-apoptotic side, and therefore their silencing promotes death, instead of senescence, after DNA damage[20].

We propose that, along with the recent discovery that senescent cells suppress the pro-apoptotic activity of p53 to remain viable[4,69], YAP–TEAD counteracts the pro-apoptotic side of p53 in senescent cells by transcriptionally repressing DDIT4 production. Therefore,

forced p53 increase, for instance by using known MDM2 inhibitors, could offer better outcomes combined with YAP–TEAD inhibition when intending to achieve senolysis[70]. In sum, we have identified YAP–TEAD as a signaling complex that allows senescent cells to remain viable by lowering ER stress through DDIT4 repression. By inhibiting this pathway, senescent cells can be selectively eliminated when their removal is advantageous.

Despite the promising effects of VPF-triggered senolysis in aged and chemotherapy-treated mice, as measured by molecular and cellular analysis of VPF actions in mouse lungs, a deeper characterization of the physiologic improvements caused by VPF is warranted. The reduction in fibrosis after VPF treatment indicates that decreasing senescence improves organ homeostasis, in keeping with many other benefits linked to senolysis in previous studies[44,56,57,70–73]. Future work should compare the senolytic effects of VPF (and more broadly, YAP–TEAD inhibitors) to those of other known senolytics, on pathophysiologic processes exacerbated by senescent cells. We postulate that suppressing YAP–TEAD may offer distinct physiologic benefits, since it exploits the dependence of senescent cells on the ER to mount the SASP, while most current senolytics target the survival–apoptosis balance that enables senescent cell viability[4,14,20,70,73,74]. In sum, our study suggests that metabolically targeting senescent cells[42] by interfering with ER biogenesis can trigger senolysis and ameliorate age-related organ fibrosis.

Methods

Cell culture, senescence induction and senescent cell detection

Human fibroblasts IMR-90 (American Type Culture Collection (ATCC), CCL-186), WI-38 (obtained from the NIGMS Human Genetic Cell Repository, Coriell Institute for Medical Research; repository ID AG06814-N) and BJ (ATCC, CRL-2522) were cultured in DMEM (Gibco) supplemented with 10% heat-inactivated fetal bovine serum (FBS), 0.5% penicillin–streptomycin, sodium pyruvate and non-essential amino acids (all from Gibco) in a 5% CO_2 incubator. HUVECs (ATCC, PCS-100-013) and HSAECs (ATCC, PCS-301-010) were cultured in their respective media (Vascular Cell Basal Medium plus Endothelial Cell Growth Kit-BBE, Airway Epithelial Cell Basal Medium plus Bronchial Epithelial Cell Growth Kit, ATCC), supplemented with 0.5% penicillin–streptomycin, sodium pyruvate and non-essential amino acids; and cultured under the same conditions (5% CO_2 incubator). Cells were kept at low population doubling levels for all the experiments in this study, unless indicated.

Cellular senescence was triggered as follows. ETIS was triggered in WI-38, BJ and IMR-90 cells after culturing for 6 to 8 d in the presence of different etoposide concentrations (50, 25 and 50 μM, respectively; Etoposide, Selleckchem). For IRIS, WI-38 cells were exposed to 15 Gy, medium was refreshed, and cells were cultured for 6 to 8 additional days. RS was achieved after repeated passaging of WI-38 cells until they reached replicative exhaustion (population doubling level ~ 55). For ETIS of HUVECs and HSAECs, cells were treated with etoposide (10 and 20 μM, respectively) for 3 d and medium was refreshed (without etoposide) until days 6 to 8. All the remaining drugs and compounds used were refreshed every 48–72 h; VPF (Selleckchem, S1786), CA3 (Selleckchem, S8661), MYF-01-37 (MedChemExpress, HY-139603), K-975 (MedChemExpress, HY-138565),

Torin1 (SelleckChem, S2827) and PtdCho (l-α-phosphatidylcholine, Sigma-Aldrich, P3782).

Transfection of siRNAs was carried out by following the manufacturer's instructions (RNAiMAX, Invitrogen). In short, cells at 50% confluency were transfected with ON-TARGETplus SMARTPool (Dharmacon) non-targeting siCtrl (D-001810-10-05), siMOB1A (L-021097-00-0005), siTEAD2 (L-012611-01-0005), siYAP1 (L-012200-00-0005), siMAP4K1 (L-003586-00-0005), siTAOK2 (L-004171-00-0005), siPERK (L-004883-00-0005), siDDIT4 (L-010855-01-0005), siTP53 (L-003329-00-0005) and siRELA (L-003533-00-0005) siRNAs at a final concentration of 25 nM. Twenty-four hours later, additional treatments were initiated as indicated, including etoposide treatment to induce senescence. Cell viability was measured by direct cell counting and represented as the percentage of remaining cells compared to the number of cells present at the beginning of the experiment. Cell counts were performed manually by using ImageJ, in at least three independent replicates. Three different fields were selected and counted for each replicate analyzed.

SA-β-gal activity was assayed using a commercial staining kit (Cell Signaling Technology, 9860) following the manufacturer's instructions.

CRISPR screen analysis

ETIS WI-38 fibroblasts (10 d in 50 μM etoposide) were transduced with the whole-genome lentiviral CRISPR-Cas9 knockout Brunello library (Addgene) at a previously optimized MOI of 0.44 (for 16 h with 1 μg ml^{-1} polybrene). Three days later, a replicate was collected and considered as $t = 0$. After incubation for an additional 14 d, the $t = 14$ samples were collected, in triplicate. A total of 40,500,000 cells transduced with 18,000,000 lentiviral particles were collected for each of the replicates. These samples were sequenced on a NextSeq 500 instrument and aligned to the sgRNA sequences contained in the Brunello CRISPR library (NGS sequencing, Cellecta). sgRNA read counts were analyzed with DESeq2 package v1.32.0 75 to calculate differential sgRNA representation and statistical significance[75]. The sgRNAs decreasing at least twofold (P value < 0.05) in $t = 14$ compared to $t = 0$ were included in the analysis through the Enrichr platform[76].

Measurement of BrdU incorporation, caspase-3/caspase-7 activity and phosphatidylcholine levels

Cells were incubated for 24 h with 4 μg ml^{-1} BrdU diluted in media. BrdU incorporation was assayed using a BrdU Cell Proliferation Assay Kit (Cell Signaling Technology, 6813) following the manufacturer's protocol.

To measure caspase-3/caspase-7 activity, cells were lysed on the plate using Caspase-Glo 3/7 Assay System (Promega) solution C, shaken for 30 s and incubated at 25 °C in the dark for 30–180 min. Luminescence was measured using a GloMax plate reader (Promega) and normalized to cell counts.

PtdCho levels were quantified by assaying cell lysates with a Phosphatidylcholine Assay Kit (Sigma-Aldrich) following the manufacturer's instructions.

RT-qPCR analysis

Tissue samples (flash-frozen) or cells were lysed in either Tri-Reagent (Invitrogen) or RLT buffer (Qiagen). Tissue samples needed an extra step for their disruption with a tissue homogenizer (Bertin Instruments). Lysates from tissues and cells were processed with the QIAcube (Qiagen) to purify total RNA, and then reverse transcribed to synthesize cDNA using Maxima reverse transcriptase (Thermo Fisher Scientific) and random hexamers. Real-time, qPCR analysis was performed using SYBR Green mix (Kapa Biosystems), and the relative mRNA levels were determined by the $2^{-\Delta\Delta Ct}$ method. All mRNAs evaluated were normalized to human *ACTB* mRNA or mouse *Actb* mRNA levels. Primers used to detect human and mouse mRNAs are specified in Supplementary Table 7.

YAP–TEAD luciferase assay

Cells were transduced at an MOI of 5 with a commercial lentiviral construct containing a luciferase reporter for TEAD activity (TEAD Luciferase Reporter Lentivirus, BPS Bioscience). Luciferase activities were measured by using a commercial kit (Steady-Glo Luciferase Assay System, Promega) and normalized to cell counts.

Western blot analysis

Protein extracts were obtained by lysing the samples with 2% SDS (Sigma-Aldrich) in 50 mM HEPES. Lysates were boiled for 5 min and sonicated, and whole-cell protein extracts were separated according to size by electrophoresis using polyacrylamide gels and transferred to nitrocellulose membranes (Bio-Rad). The membranes were then blocked for 1 h with 5% non-fat dry milk in TBST and immunoblotted with primary antibodies recognizing phosphorylated AKT (Ser473; Cell Signaling Technology, 4060S), ACTB (β-actin C4, Santa Cruz Biotechnology, sc-47778), phosphorylated EIF2A (S51; Abcam, ab32157), ATF4 (Cell Signaling Technology, 97038), phosphorylated p70 S6K (Thr389; Cell Signaling Technology, 9234), phosphorylated mTOR (Ser2448; Cell Signaling Technology, 5536), XBP1s (Cell Signaling Technology, 12782), ATF6 (Cell Signaling Technology, 65880), phosphorylated YAP (S127; Cell Signaling Technology, 13008), phosphorylated MOB1 (Thr35; Cell Signaling Technology, 8699), MOB1 (Cell Signaling Technology, 13730), lipin-1/LPIN1 (Cell Signaling Technology, 5195) and CCTα/PCYT1A (Cell Signaling Technology, 6931). All antibodies were incubated for 16 h at 4 °C at a 1:1,000 dilution in 3% BSA in TBST. ACTB was used as a loading control for all western blots, at a 1:4,000 dilution in 3% BSA in TBST. After incubation with the appropriate horseradish peroxidase-conjugated secondary antibodies (Jackson ImmunoResearch; 115-035-003 and 111-035-003, goat anti-mouse and goat anti-rabbit, respectively, in 5% non-fat dry milk in TBST, 1:10,000), the chemiluminescent signals were obtained by using the Chemidoc system (Bio-Rad).

Co-immunoprecipitation

To perform co-IP analysis of the interaction between YAP and TEAD, we lysed 3 million cells per replicate with RIPA buffer plus Protease/Phosphatase Inhibitor Cocktail (Cell Signaling Technology) on ice. Samples were then sonicated twice for 20 s, centrifuged for 10 min at 10,000*g* at 4 °C, and the resulting supernatants (1 mg each) were incubated for 16

h at 4 °C (in rotation) with either TEAD antibody (Cell Signaling Technology, 13295) or an IgG isotype control (Cell Signaling Technology, 3900), using 0.5 μg of each antibody along with 250 μg of Pierce Protein A/G Magnetic Beads (Thermo Fisher). Antibody quantities for immunoprecipitation were optimized and adjusted to account for the different TEAD levels between control and VPF-treated WI-38 cells. After three rounds of washes, the samples were eluted in SDS lysis buffer and studied by regular western blot analysis. The antibodies used for immunoblotting recognized YAP (Cell Signaling Technology, 14074) or TEAD (Cell Signaling Technology, 13295). Densitometry analysis of the signals on western blots was performed with ImageJ.

Endoplasmic reticulum tracker staining

ER Tracker Red (BODIPY TR glibenclamide) was from Thermo Fisher. Briefly, cells were incubated with 0.5 μM ER Tracker Red for 30 min and fixed with 4% paraformaldehyde; micrographs were taken with a fluorescence microscope (BZ-X Analyzer, Keyence). The relative ER-positive areas were measured with ImageJ.

Mice and mouse histology

All mouse work, including the import, housing, experimental procedures and euthanasia, was performed under an Animal Study Proposal (ASP no. 476-LGG-2023), reviewed and approved by the Animal Care and Use Committee of the National Institute on Aging (NIA), National Institutes of Health (NIH). C57BL/6JN mice were provided Inotiv 2018SX diet ad libitum and maintained under a 12 h–12 h light–dark cycle. All drugs included in the study were delivered intraperitoneally, using a maximum volume of 80 μl. Doxorubicin-induced senescence was triggered after a single dose of doxorubicin (10 mg per kg body weight, Selleckchem) and studied >10 d later. DMSO, VPF (50 mg per kg body weight, Selleckchem) or ABT-737 (25 mg per kg body weight, MedChem-Express) were used in mice treated with doxorubicin or 22-month-old mice following different regimens as specified (Results). Young control mice followed the DMSO regimen once and were euthanized 1 week later, similarly to the aged mice.

For histology, tissues were immediately fixed in 4% paraformaldehyde in PBS at 4 °C for 16 h. The next day, samples were cryoprotected in a 30% sucrose solution in PBS at 4 °C for 16 h, embedded in optimal cutting temperature (OCT) compound and stored at −80 °C. Samples were then cut and mounted, and the different downstream assays were performed. Immunofluorescence staining was performed with antibodies that recognized phosphorylated EIF2A (S51; Abcam, ab131505), CDKN2A/p16INK4a (Abcam, ab54210) or p21 (Abcam, ab107099), at a 1:100 dilution. Collagen deposition was evaluated by staining tissues with MTC. Relative areas of fibrosis were calculated by measuring the area positive for MTC (blue) divided by the area of total tissue (dark red). All the measurements were performed with ImageJ in different fields for each of the mice included in the analysis. All the tissue staining procedures were performed commercially by iHisto (https://www.ihisto.io/).

Analysis of proteins in mouse serum and conditioned medium

Mouse blood was extracted, allowed to clot for 2 h at 25 °C and centrifuged for 20 min at 2,000*g*. The serum (supernatant) was collected and frozen at −80 °C. Before the assays, serum was thawed and centrifuged at 16,000*g* for 4 min. Blood urea nitrogen and aspartate transaminase were measured in a Dimension EXL Integrated Chemistry system (Siemens). A custom murine Luminex Assay kit was designed by R&D Biosystems to include GDF15 for mouse serum analysis. Conditioned medium was collected from human cell cultures 48 h after adding fresh medium and was analyzed with a custom human Luminex assay platform designed to include human IL1A, IL6, CXCL1, CXCL2, CCL2, LIF, IGFBP-rp1, BDNF, BMP4, FGF basic and GDF15. Serum or medium was diluted at a 1:2 ratio using Calibrator Diluent RD6–52. Standards, blanks and serum were incubated with the microparticle cocktail for 2 h at 25 °C, and then incubated with a biotin antibody cocktail for 1 h. A final incubation of 30 min with Streptavidin-PE was carried out with shaking at 25 °C before plate analysis on the Bio-Rad Bio-Plex 200 instrument. Every incubation step was followed by three washes with wash buffer. The results were analyzed with the Bio-Plex Manager software.

Transmission electron microscopy

For TEM visualization, cultured cells were fixed at room temperature using 2.5% glutaraldehyde in 0.1 M sodium cacodylate buffer, pH 7. Cells were then scraped, gently spun down in 1.5-ml microcentrifuge tubes and post-fixed in 1% osmium tetroxide for 1 h at 4 °C in the same buffer. Samples were dehydrated in increasing percentages of ethanol and embedded in Embed 812 resin (Electron Microscopy Sciences) through a sequence of resin resin-propylene oxide gradients until reaching pure resin. Blocks were formed in fresh resin contained in the same conical tubes, and the resin was polymerized for 48–72 h at 65 °C. Blocks were trimmed and sectioned in an EM UC7 ultramicrotome (Leica Microsystems) to obtain both semi-thick (0.5–1 μm width) and ultrathin (40–60 nm width) sections. Semi-thick sections were mounted on glass slides and stained with 1% toluidine blue in a 1% borax aqueous solution for 2 min and visualized using a Leica AXIO Imager light microscope for quality control. Ultrathin sections were stained with uranyl acetate and lead citrate and then imaged on a Talos L120C TEM with a 4K Ceta CMOS camera. Maximal ER cisternae thickness per cell was measured with ImageJ by measuring the longest distance between ER cisternae walls in each cell. A disorganization score was given according to the level of disorganization shown by the ER in each cell (ranked 1 to 4). Parameters such as continuity or shape were considered to determine the score. Thirty cells were analyzed for each condition.

ChIP-qPCR analysis

Chromatin immunoprecipitation and subsequent qPCR analysis were performed by using SimpleChIP Plus Enzymatic Chromatin IP Kit (Cell Signaling) following the manufacturer's instructions. Briefly, 10 μg of sheared chromatin (150–900 bp) was incubated overnight with 0.25 μg of either anti-YAP (Cell Signaling, 14074) or Normal Rabbit IgG (Cell Signaling, 2729). The eluted DNA was de-crosslinked, column-purified and quantified by RT-qPCR analysis. Data were displayed by normalizing the percentage of input

recovered by YAP antibody to the percentage of input recovered by IgG control for each replicate (not shown in the graphs). Negative control used is a primer set (ACCAACACTCTTCCCTCAGC and TTATTTTGGTTCAGGTGGTTGA) that amplifies a region of Chromosome 10 known to be unrelated to YAP–TEAD binding[16]. Primers for DDIT4 gene (TGTTTAGCTCCGCCAACTCT and CACCCCAAAAGTTCAGTCGT) were designed to target a region in exon 2 that is at a distance from YAP binding sequence in the regulatory region of the *DDIT4* gene, shorter than 900 bp.

RNA-seq analysis

Bulk RNA was extracted with RLT buffer (Qiagen) using the QIAcube system (Qiagen) following the RNeasy Plus protocol. RNA quality and quantity were assessed using the Agilent RNA 6000 nano kit on the Agilent Bioanalyzer. High-quality RNA (125 ng) was used for the library preparation using the Illumina TruSeq Stranded mRNA Library preparation kit following the manufacturer's protocol (Illumina). The quality and quantity of the libraries were checked using the Agilent DNA 1000 Screen Tape on the Agilent Tapestation. Paired-end sequencing was performed for 103 cycles with an Illumina NovaSeq sequencer. BCL files were de-multiplexed and converted to FASTQ files using bcl2fastq program (v2.20.0.422). FASTQ files were trimmed for adaptor sequences using Cutadapt version v1.18 and aligned to human genome hg19 Ensembl v82 using STAR software v2.4.0j. Gene counts were generated using featureCounts (v1.6.4) software and normalized with DESeq2 package (v1.32.0). Further analysis of the transcriptomic differences among samples was performed using normalized counts in the GSEA platform[77]. YAP–TEAD targets were identified by both existing evidence on the literature and analysis with MAGIC database[78].

scRNA-seq libraries from cultured cells were prepared as instructed in the Chromium Next GEM Single Cell 3′ Reagent Kits v3.1 (10x Genomics) user guide. Briefly, ETIS cells (untreated and VPF-treated for 72 h) were trypsinized, washed with PBS, and resuspended in 10% FBS and 0.1 mM EDTA in PBS at a concentration of 900–1,000 cells per microliter. The resulting single-cell suspension was loaded into a Chromium Next GEM Chip G (10x Genomics), and GEMs were generated with the Chromium Single Cell Controller (10x Genomics). Libraries were prepared using 11 and 13 cycles for cDNA amplification and Sample Index PCR (Single Index Kit T Set A, 10x Genomics), respectively, and subjected to paired-end sequencing on a SP100 flow cell on an Illumina NovaSeq platform. Raw single-cell RNA-seq data were processed through Cell Ranger software 6.0.0 (10x Genomics) and sequencing reads mapped to a pre-built human reference (GRCh38; version 2020-A, 10x Genomics). Filtered matrix files generated by Cell Ranger were processed using R (version 4.2.2) and the Seurat R package (version 4.2.0). Cells expressing >200 transcripts and <15% of mitochondrial transcripts were included in the analysis. Untreated and VPF-treated samples were processed separately; both were log-normalized, scaled to 10,000, dimensionally reduced by principal component analysis (PCA) using the top 2,000 highly variable features and visualized by performing UMAP. Both samples were then integrated using the Seurat CCA method. The integrated data were scaled and dimensionally reduced using PCA and UMAP as above. Single cells in the integrated data were clustered into six subgroups using $r =$

0.2 resolution. The gene set used for analyzing ER stress was downloaded from MsigDB (GOBP_RESPONSE_TO_ENDOPLASMIC_RETICULUM_STRESS). A list of 132 SASP-related genes included for analysis was obtained after filtering out the secretory genes not detected by bulk RNA-seq in WI-38 cells and were used as a broader gene set for SASP (Supplementary Table 3). The average expression levels of each gene set on single cells were calculated using the AddModuleScore function in Seurat. The returned module scores in single cells in each cluster were averaged, scaled and were subsequently used for gene-set activity comparison in dot plots.

scRNA-seq analysis from mouse lungs was performed after dissociating two pieces of left lobes (25 mg each from two different mice) previously perfused by injecting 1 ml PBS through the right ventricle of the heart. Each pool of cells in 50 mg of lung tissue was placed into a Miltenyi C tube filled with 2 ml of a mixture of RPMI media, 0.2 mg ml^{-1} Liberase TL and 0.1 mg ml^{-1} elastase. The following program was then run in the Gentlemacs Octodissociator (Miltenyi) at a constant temperature of 37 °C: 20 min, 50 r.p.m.; 30 s, 2,000 r.p.m. (clockwise); 30 s, 2,000 r.p.m. (counterclockwise). Samples were then passed through a MACS SmartStrainer (70 μm), centrifuged and the remaining pellets resuspended in RPMI + 20% FBS. After dissociation, cells were first incubated for 5 min with 5 μl of TruStain FcX PLUS (anti-mouse CD16/CD32) blocking reagent followed by a 15-min incubation with 5 μl of anti-mouse Ter119-Pacific Blue and 5 μl of anti-mouse CD45-PE/Cyanine7 for 15 min at 25 °C in the dark. Cells were then washed with 1 ml of DMEM supplemented with 15% FBS and resuspended in 500 μl of DMEM supplemented with 15% FBS, 2 μg ml^{-1} of propidium iodide and 50 mM EDTA. Lastly, 25,000 cells were sorted using FACS Aria FUSION (BD Bioscience). Single-cell libraries were prepared in two repeats per experimental condition (eight samples) and constructed using the Chromium Next GEM Single Cell 3′ Kit v3.1 with Chromium Next GEM Chip G Single Cell Kit in a Chromium Controller (10x Genomics) following the manufacturer's protocol. Pre-processing of sequencing results and generation of count matrices were performed using the Cell Ranger version 6.1.1 (10x Genomics) with pre-built annotation platform mm10-2020-A. The resulting matrix files were processed using R (version 4.2.3) and the Seurat R package (version 4.3.0). Cells with >200 and <6,000 nFeature_RNA, <30,000 nCount_RNA and <25% of mitochondrial genes were kept for the downstream analysis. Once filtered, each sample was log-normalized with the LogNormalize method, and the top 2,000 highly variable genes were used to compute inter-sample anchors for integration. After that, all eight samples were integrated, scaled and subjected to PCA dimensional reduction. The top 40 principal components, determined by the ElbowPlot method, were applied to find nearest neighbors and UMAP data visualization in a two-dimensional space. Clustering with a resolution of 0.2 defined 28 different clusters. Marker genes that characterized cells of each cluster compared to all other clusters were identified with FindAllMarkers function. Different cell types were then identified with Enrichr by introducing each cluster's markers. Once designated, the cell clusters were curated with the existing literature. To obtain the $-\log_{10}(P\text{ value})$ used in Fig. 4i, the top 200 transcripts (obtained from the log1p average expression values for each condition per cluster) increased in old DMSO at least 2-fold relative to young DMSO and 1.5-fold relative to both old VPF and old ABT-737 were included for the analysis with Enrichr. The *P* values obtained there were used to create a heat

map, and the exact gene sets for which the values were given are specified in Supplementary Table 4. The log1p average expression values were also used to carry out GSEA displayed in Fig. 4j and Extended Data Fig. 5f. Sequencing data are deposited in the Gene Expression Omnibus repository under accession number GSE221254.

Statistics and reproducibility

Data are represented as the means ± s.d. of at least $n = 3$ independent experiments (except for the ChIP-qPCR experiments, which were performed in duplicate). Individual data points are shown in all the bar plots. Significance was determined using two-tailed Student's *t*-test (*$P < 0.05$, **$P < 0.01$, ***$P < 0.001$) for cell culture experiments, while one-way analysis of variance (*$P < 0.05$, **$P < 0.01$, ***$P < 0.001$) was used for in vivo experiments. All the statistical analyses were carried out with Prism 9, except for the GSEA plots, which were prepared using the GSEA platform. No statistical methods were used to predetermine sample sizes, but our sample sizes are similar to those previously published[14,20]. Data distribution was assumed to be normal, but this was not formally tested. Data collection and analysis were performed blind to the experimental conditions whenever possible. No data points were excluded from any of the graphs shown.

Reporting summary

Further information on research design is available in the Nature Portfolio Reporting Summary linked to this article.

Extended Data

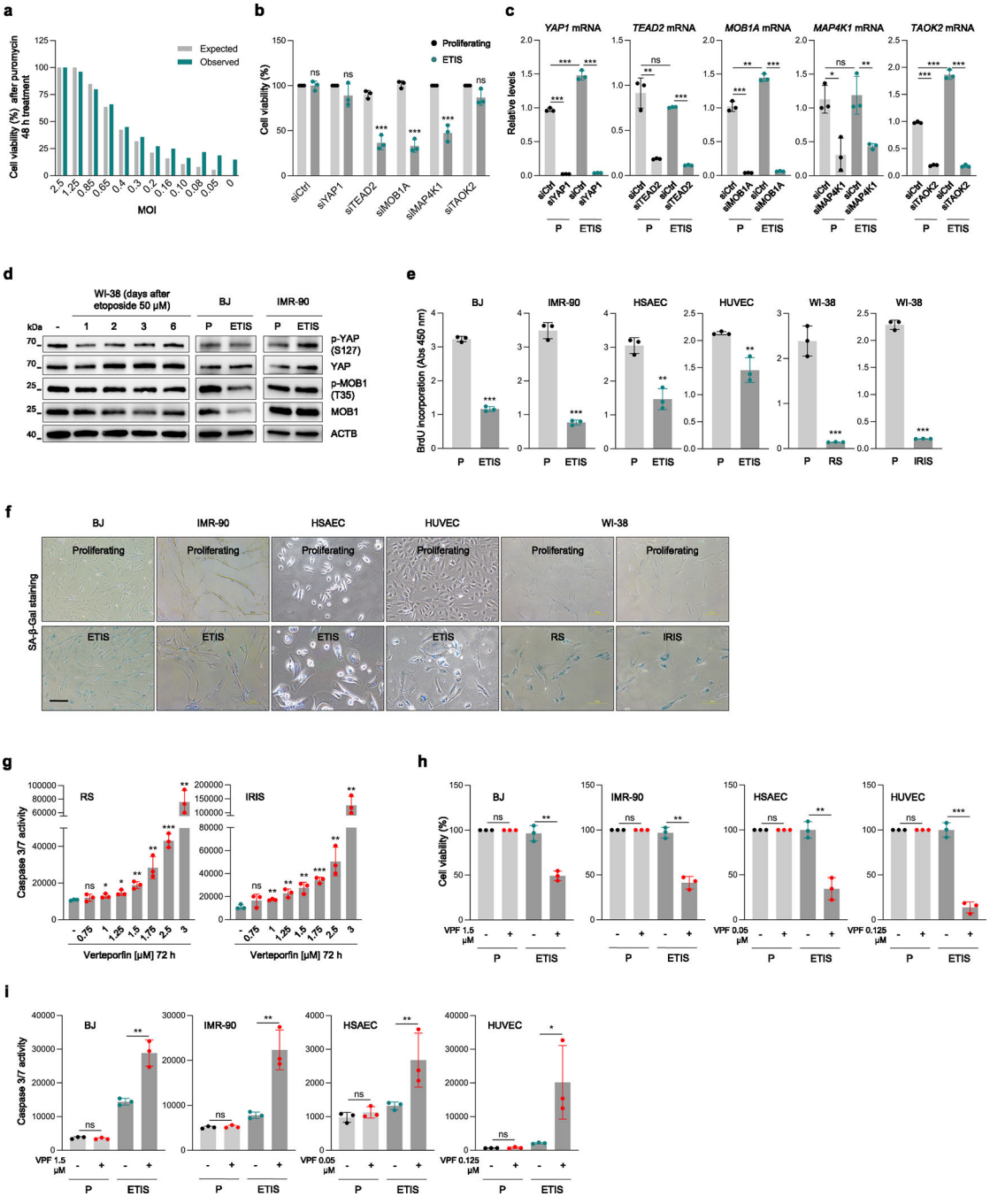

Extended Data Fig. 1 |. CRISPR screen optimization, validation, and YAP-TEAD inhibition in other senescence models.

a, Cell viability assessment by direct cell counting of senescent WI-38 cells treated with puromycin (1 μg/ml, 48 h) 72 h after being transduced with the Brunello library at the indicated MOIs. The gray bars represent the expected viability if the transduction efficiency was complete while the teal bars represent the viability observed for each of the MOIs after puromycin treatment. **b**, Cell viability as assessed by direct cell counting of WI-38 cells

transfected with the indicated siRNAs and rendered senescent after treatment with etoposide for 6 days (ETIS). **c**, Analysis of the levels of the indicated mRNAs in proliferating (P) or ETIS WI-38 cells transfected with the indicated siRNAs 24 h before either treatment with etoposide (50 μM) or no treatment, and culture for an additional 6 days. **d**, Representative western blot analysis (n = 3 independent experiments) of the levels of phosphorylated YAP (S127), YAP, phosphorylated MOB1 (T35), MOB1, and ACTB levels at the indicated conditions. e, f, Analysis of BrdU incorporation (**e**) and SA-β-Gal staining (**f**) in the indicated cell types, rendered senescent by etoposide (ETIS), ionizing radiation (IRIS), or replicative exhaustion (RS). Scale bar 100 μm. **g**, Caspase 3/7 activity measured in RS and IRIS WI-38 cells treated for 72 h with the indicated doses of Verteporfin (VPF). **h**, **i**, Cell viability as assessed by direct cell counting (**h**) and Caspase 3/7 activity measurement (**i**) for the indicated models of senescence along with proliferating controls, after either no treatment or treatment with VPF for 72 h at the indicated doses. Graphs in (**b**, **c**, **e**, **g**–**i**) represent the means and each individual value as a dot ±s.d. n = 3 independent replicates; significance (*P < 0.05, **P < 0.01, ***P < 0.001) was determined using two-tailed Student's t-test. Unless indicated, statistical tests were performed relative to untreated or proliferating controls.

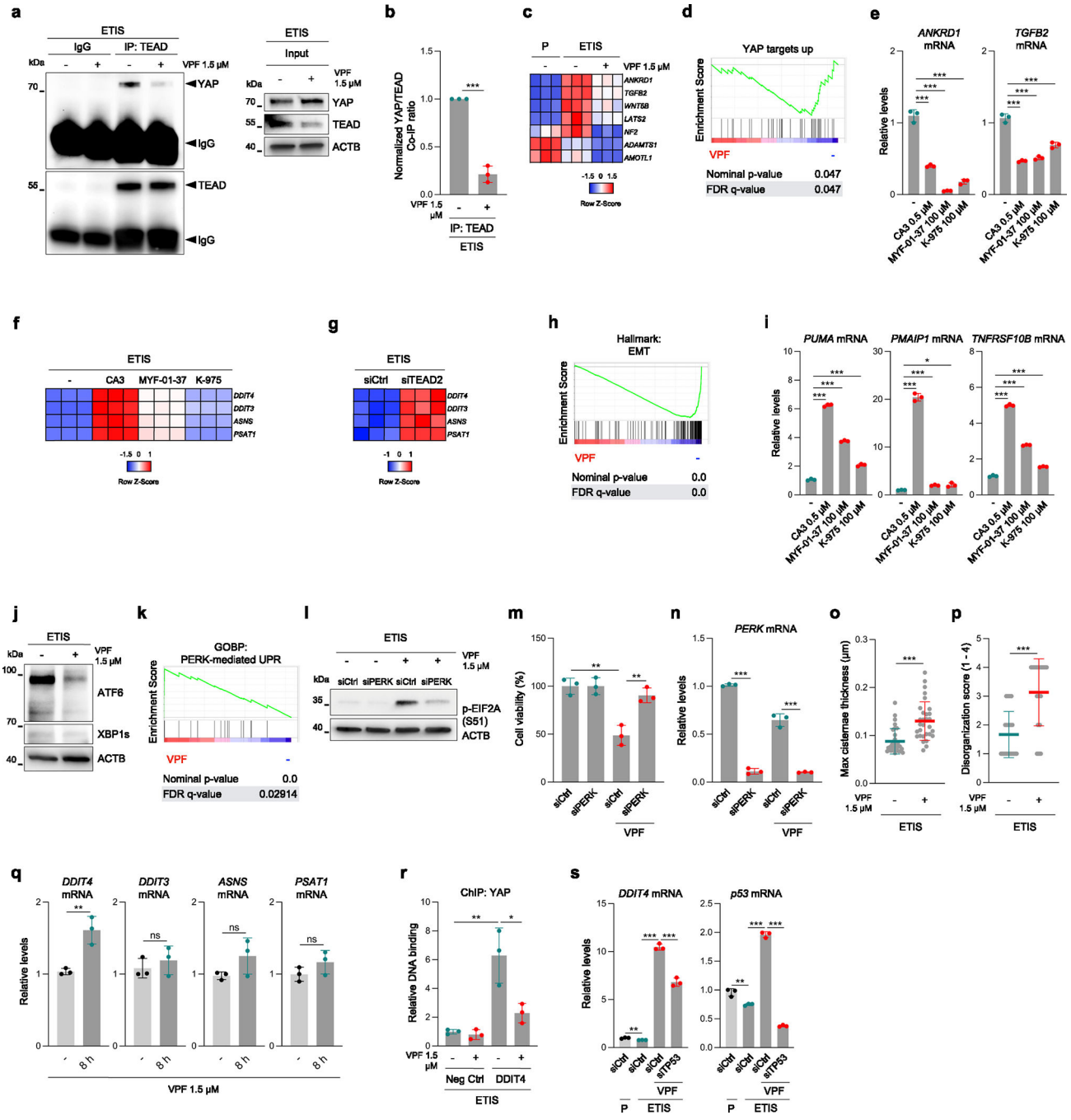

Extended Data Fig. 2 |. Extended analysis of YAP-TEAD inhibition.

a, **b**, Representative western blot analysis (**a**) and quantification (**b**) of the levels of YAP and TEAD proteins after immunoprecipitation experiments with the indicated antibodies (IgG or anti-TEAD) in ETIS WI-38 fibroblasts that were either untreated or treated with VPF for 48 h. IgG bands are indicated with arrows placed on the left side of the panel. Inputs are also included. **c**, Heat map displaying the differential expression of the YAP–TEAD-dependent transcripts (by row Z-Score) in the conditions described in (**a**). Proliferating untreated cells were included as a baseline control. **d**, GSEA of the association

(enrichment score) with the gene set ‘YAP1_up’ of ETIS WI-38 cells treated with VPF (48 h) compared to untreated senescent cells (−). **e**, RT-qPCR analysis of the levels of ANKRD1 and TGFB2 mRNAs in ETIS WI-38 cells after treatment for 48 h with the indicated YAP–TEAD inhibitors. Untreated controls were also included for comparison. **f**, Heat map representing the differential expression (Row Z-Score) among the conditions described in (**e**) for the indicated transcripts. **g**, Heat map displaying the differential expression (Row Z-Score) of the indicated transcripts in siCtrl and siTEAD2 ETIS WI-38 cells. **h**, GSEA of the association with the gene set ‘Hallmark: Epithelial-Mesenchymal Transition’ for the conditions described in (**d**). **i**, RT-qPCR analysis of the indicated pro-apoptotic mRNAs for the conditions described in (**e**). **j**, Representative Western blot (n = 3 independent experiments) of the levels of ATF6, XBP1s, and loading control ACTB for the conditions described in (**d**). **k**, GSEA plot showing the association (enrichment score) of the gene set ‘GOBP: PERK-mediated UPR’ with the conditions described in (**d**). **l**, Western blot analysis of the levels of phosphorylated EIF2A (S51) and loading control ACTB in WI-38 cells transfected with siCtrl or siPERK, rendered senescent with etoposide (ETIS) and then either left untreated or treated with 1.5 μM VPF for 48 h. **m**, **n**, Cell viability assessment by direct cell counting (**m**) and RT-qPCR analysis of PERK mRNA levels (**n**) in the conditions described in (**l**), but here treated with VPF for 72 h. **o**, **p**, Maximal cisternae thickness (**o**) and disorganization score (**p**) as measured by TEM in the groups described in (**c**). Thirty cells were analyzed for each condition. **q**, RT-qPCR analysis of the indicated transcripts either untreated or treated with 1.5 μM VPF for 8 h. **r**, Relative binding to the regulatory region of the DDIT4 gene or a negative control (Neg Ctrl) DNA in YAP ChIP samples of ETIS WI-38 cells that were untreated or treated with 1.5 μM VPF (48 h). **s**, RT-qPCR analysis of the levels of *DDIT4* and *p53* mRNAs in WI-38 cells transfected with the indicated siRNAs, rendered senescent with etoposide (ETIS) and either left untreated or treated with 1.5 μM VPF for 48 h. Proliferating WI-38 cells transfected with siCtrl were included as controls. Graphs in (**b**, **e**, **i**, **m**, **n**, **q**–**s**) display the means and the individual values as dots ±SD n = 3 independent replicates; graphs in (**o**, **p**) show the means and the individual values as dots ±s.d. of n = 30 different cells. Significance (*P < 0.05, **P < 0.01, ***P < 0.001) was calculated using two-tailed Student’s t-test.

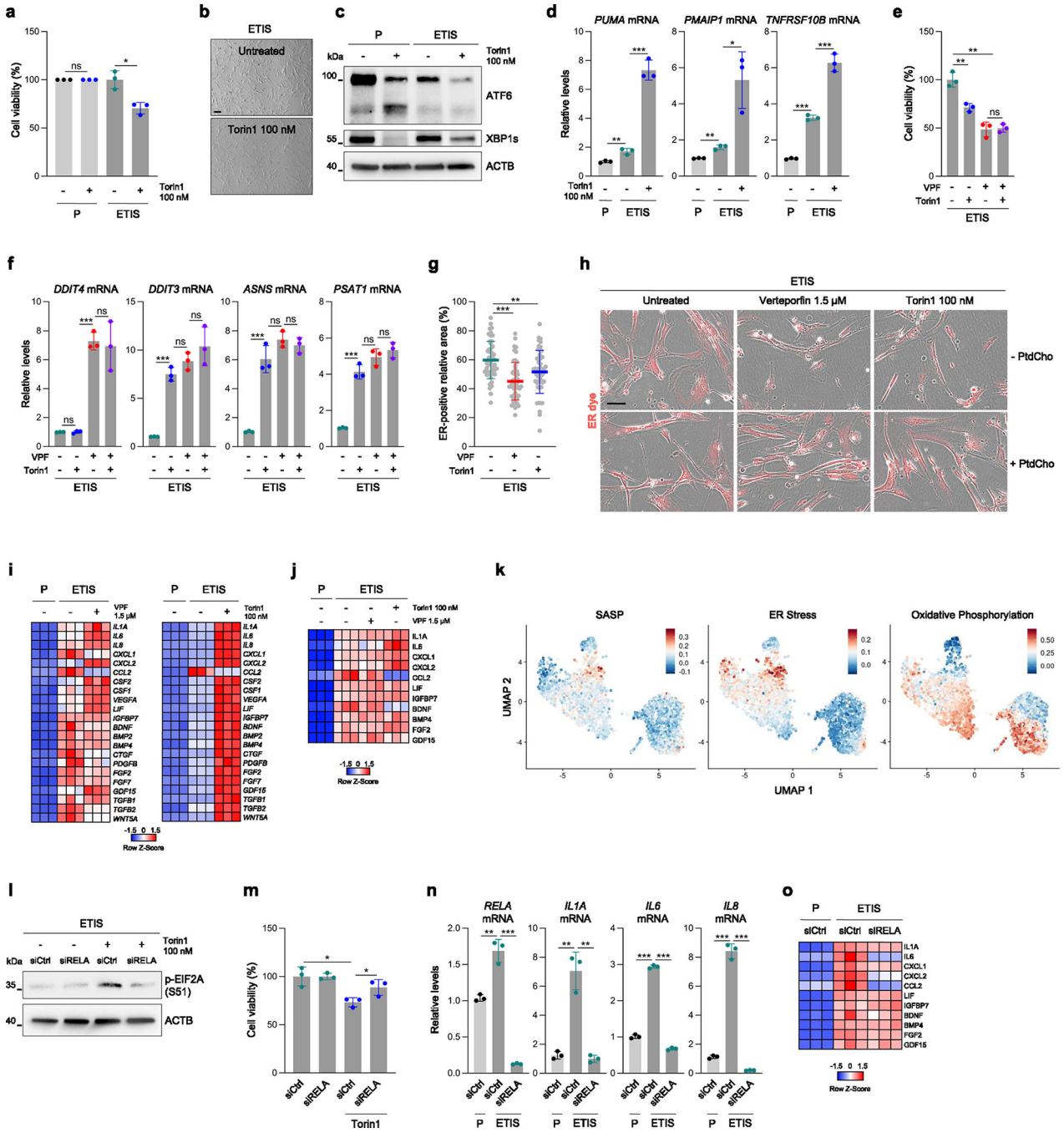

Extended Data Fig. 3 |. Analysis of mTOR inhibition and VPF treatment on ER stress in senescent cells.

a, Cell viability as assessed by direct cell counting of proliferating (P) or ETIS WI-38 fibroblasts that were either left untreated or treated with 100 nM Torin1 for 72 h. **b**, Representative micrographs showing the differences in viability in the conditions from (**a**). Scale bar, 100 μm. **c**, Western blot analysis of the levels of ATF6, XBP1s, and ACTB in the conditions described in (**a**), at 48 h instead. **d**, RT-qPCR analysis of the levels of PUMA, PMAIP1, and TNFRSF10B mRNAs in the conditions described in (**c**). Untreated P cells

were included as baseline controls. **e**, Direct cell counting after treating as indicated for 72 h (1.5 μM VPF, 100 nM Torin1, or both) in ETIS WI-38 cells. **f**, RT-qPCR analysis of the indicated transcripts for the treatments described in (**e**), in this case for 48 h. **g**, Dot plot representation of the values calculated for the ER-positive relative area per cell (60 cells per condition) in ETIS WI-38 cells either untreated or treated with VPF (1.5 μM) or Torin1 (100 nM) for 48 h. **h**, Micrographs showing the areas corresponding to the endoplasmic reticulum (ER) in red for the indicated treatments as in (**g**). Phosphatidylcholine (PtdCho) was simultaneously supplemented at 50 μM where indicated. Scale bar, 100 μm. **i**, Heat map representation of the differences in SASP mRNA levels represented by row Z-Score for the indicated transcripts when comparing the conditions described in (**g**). Untreated P WI-38 cells were included as baseline controls. **j**, Heat map of the row Z-Score calculated for the differences in the secretion of the indicated SASP members among the groups described in (**g**), including proliferating (P) WI-38 cells as a control for baseline secretion. **k**, UMAP plot representation of the scRNA-seq data from ETIS WI-38 cells (no VPF treatment) showing the expression score specified in the legends, associated with the indicated gene sets (SASP, a custom gene set of 132 markers; ER stress, GOBP: Response to ER stress; and Oxidative Phosphorylation, Hallmark: Oxidative Phosphorylation). **l**, Western blot analysis of phosphorylated EIF2A (S51) and ACTB levels in WI-38 cells transfected with the indicated siRNAs, rendered senescent by treatment with etoposide for 6 days, and then either left untreated or treated with 100 nM Torin1 for 48 h. **m**, Cell viability measurement by direct cell counting of the conditions described in (**l**), here treated for 72 h. **n**, **o**, RT-qPCR analysis (**n**) and Bioplex analysis of the conditioned media (**o**) to assess SASP production and secretion in WI-38 cells transfected with siCtrl or siRELA, and rendered senescent with etoposide for 6 days. Proliferating controls transfected with siCtrl siRNA were included. Graphs in (**a**, **d**–**f**, **m**, **n**) represent the means and individual values (dots) of n = 3 independent replicates; plot in (**g**) shows the individual values of 20 different cells from each of the 3 independent replicates analyzed, making a total 60 individual values; Significance (*P < 0.05, **P < 0.01, ***P < 0.001) was calculated using two-tailed Student’s t-test.

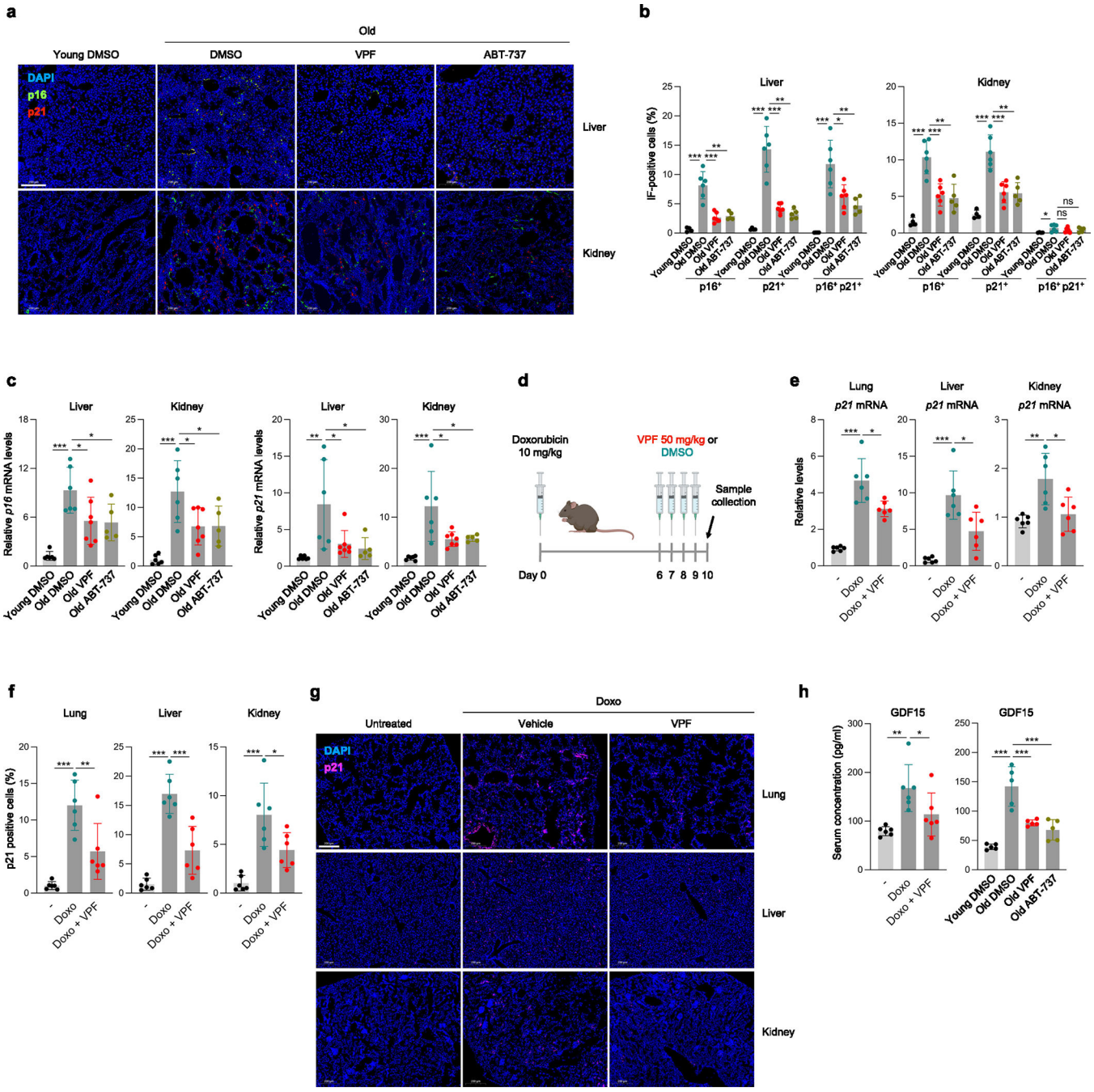

Extended Data Fig. 4 |. Analysis of senescence markers in naturally aged and doxorubicin-treated mice.

a Representative immunofluorescence images of p21 (red) and p16 (green) in mouse liver and kidney from the groups described in Fig. 4a. Scale bar (white), 200 μm. **b**, Quantification of the percentage of p16-positive, p21-positive, or p16/p21 double-positive cells in the liver and kidney samples represented in (**a**). **c**, RT-qPCR analysis of *p16* and *p21* mRNA levels (normalized to Actb mRNA) in liver and kidney for the conditions described in Fig. 4a. **d**, Schematic representation of the treatment regimen carried out to trigger doxorubicin-induced senescence in vivo in mice (10 mg/kg), along with 4 consecutive

treatments with DMSO (Vehicle) or VPF (50 mg/kg) from day 6 onward. Samples were collected at day 10 after doxorubicin treatment. **e**, RT-qPCR analysis of *p21* mRNA levels in lung, liver, and kidney from the groups described in (**d**). Untreated mice were included as baseline controls. **f**, **g**, Quantification (**f**) and representative images (**g**) of p21 immunofluorescence in the conditions described in (**d**). Scale bar (white), 200 μm. **h**, Serum measurement of GDF15 levels for the experimental groups described in (**d**, left, and Fig. 4a, right). Graphs in (**b**, **c**) display the means and the individual values as dots ± s.d. of the included mice (more details in Supplementary Table 6), while graphs in (**e**, **f**, **h**) display the means and the individual values as dots ± s.d. of n = 6 mice per group; significance (*P < 0.05, **P < 0.01, ***P < 0.001) was calculated using one-way ANOVA.

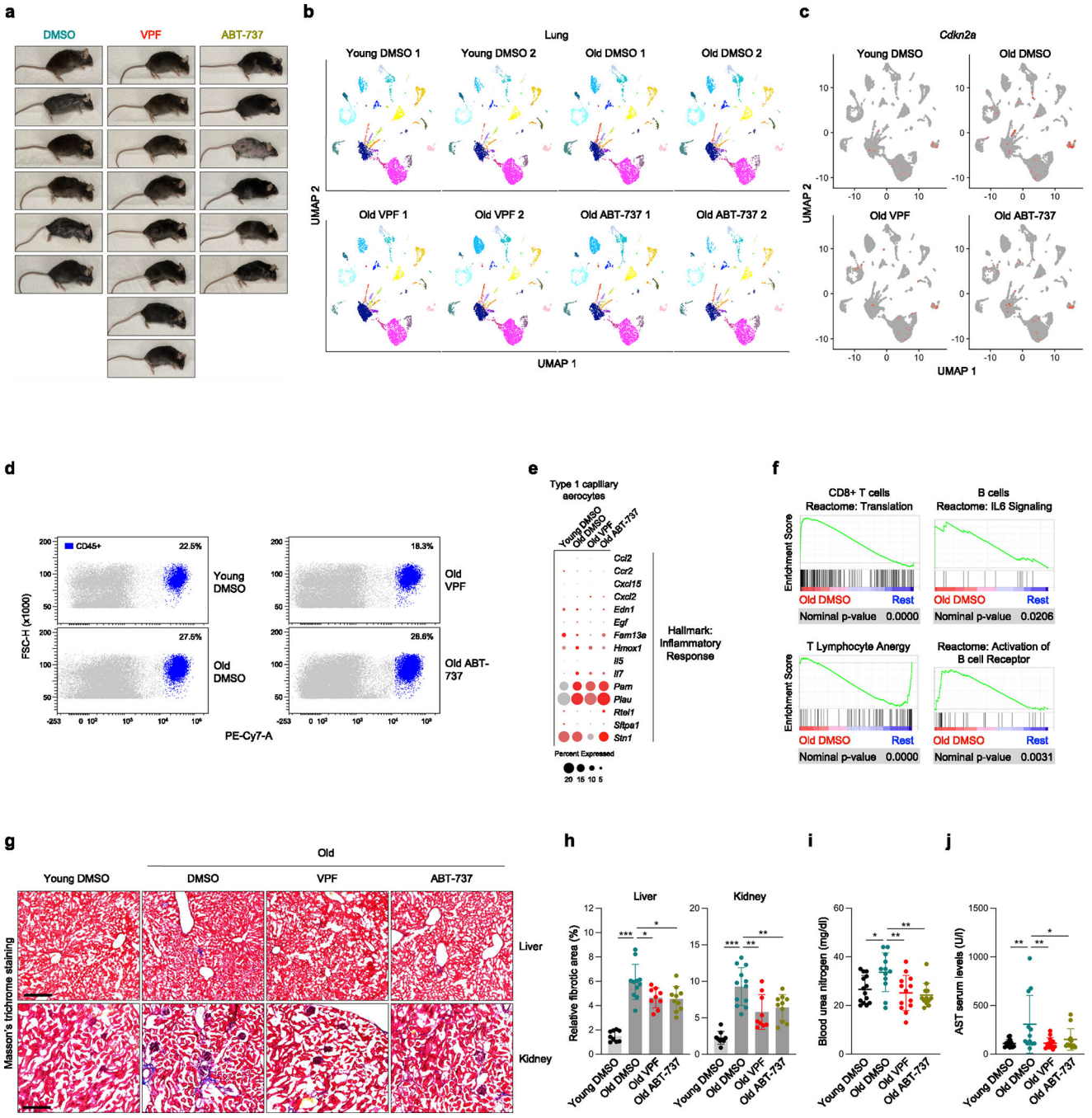

Extended Data Fig. 5 |. Physiological benefits of senolytic ABT-737 and VPF treatments in naturally aged mice.

a, Pictures of the 24 m.o. mice from the different groups described in Fig. 4a at the end of the experiment. **b**, UMAP clustering of the scRNA-seq performed in lungs from the indicated groups. **c**, Feature plot displaying *Cdkn2a* mRNA expression in the indicated experimental groups. Each plot was obtained by merging the two samples sequenced for each experimental group, shown in (**b**). **d**, Plots displaying the signals obtained through flow cytometry analysis of single-cell lung suspensions from the indicated groups. FSC-H axis

represents the signals obtained for the forward scatter, while the PE-Cy7-A axis corresponds to CD45 staining with such fluorophore. Cells considered CD45+ are colored in blue, and the percentages are specified on the top right corner of each box. **e**, Dot plot displaying the association of the indicated cell types and conditions with the top 15 transcripts from Hallmark: Inflammatory Response gene set. The size of the dots represents the percentage of cells expressing such transcript while the intensity of red indicates the relative expression value. **f**, GSEA plots displaying the association of the indicated cell types from Old DMSO condition (compared to the rest of the experimental groups) with the indicated gene sets (Reactome: Translation; Safford T Lymphocyte Anergy; Reactome: Interleukin 6 Family Signaling; Reactome: Antigen Activates B cell Receptor BCR Leading To Generation Of Second Messengers). **g**, **h**, Masson's trichrome (MTC) staining performed in liver and kidney from the indicated groups, representative images of MTC staining (**g**) in blue, and quantification of the blue area present at each sample divided by the total area in red (**h**). Scale bar, 200 μm. **i**, **j**, Serum analysis of blood urea nitrogen (**i**) and AST (**j**) levels for the indicated experimental groups. Plots in (**h**–**j**) represent the means and the individual values as dots ± s.d. of the included mice (more details in Supplementary Table 6); significance (*P < 0.05, **P < 0.01, ***P < 0.001) was calculated using one-way ANOVA.

Supplementary Material

Refer to Web version on PubMed Central for supplementary material.

Acknowledgements

This research was supported in its entirety by the NIA IRP, NIH. The funders had no role in study design, data collection and analysis, decision to publish or preparation of the manuscript.

Data availability

RNA-seq fastq files generated for this study are available at the Gene Expression Omnibus under accession number GSE221254 to provide access to all datasets in this study. YAP–TEAD targets were identified by both existing evidence on the literature and curation with MAGIC database. Source data are available with this paper.

References

1. Gorgoulis V et al. Cellular senescence: defining a path forward. Cell 179, 813–827 (2019). [PubMed: 31675495]
2. Di Micco R, Krizhanovsky V, Baker D & d'Adda di Fagagna F Cellular senescence in ageing: from mechanisms to therapeutic opportunities. Nat. Rev. Mol. Cell Biol. 22, 75–95 (2021). [PubMed: 33328614]
3. Gasek NS, Kuchel GA, Kirkland JL & Xu M Strategies for targeting senescent cells in human disease. Nat Aging 1, 870–879 (2021). [PubMed: 34841261]
4. Baar MP et al. Targeted apoptosis of senescent cells restores tissue homeostasis in response to chemotoxicity and aging. Cell 169, 132–147 (2017). [PubMed: 28340339]
5. Kirkland JL & Tchkonia T Senolytic drugs: from discovery to translation. J. Intern. Med. 288, 518–536 (2020). [PubMed: 32686219]
6. Lipina C & Hundal HS Is REDD1 a metabolic eminence grise? Trends Endocrinol. Metab. 27, 868–880 (2016). [PubMed: 27613400]

7. Doench JG et al. Optimized sgRNA design to maximize activity and minimize off-target effects of CRISPR–Cas9. Nat. Biotechnol. 34, 184–191 (2016). [PubMed: 26780180]
8. Dupont S et al. Role of YAP/TAZ in mechanotransduction. Nature 474, 179–183 (2011). [PubMed: 21654799]
9. Srikantan S, Marasa BS, Becker KG, Gorospe M & Abdelmohsen K Paradoxical microRNAs: individual gene repressors, global translation enhancers. Cell Cycle 10, 751–759 (2011). [PubMed: 21311220]
10. Lee DH et al. LATS-YAP/TAZ controls lineage specification by regulating TGFβ signaling and Hnf4α expression during liver development. Nat. Commun. 7, 11961 (2016). [PubMed: 27358050]
11. Chan M et al. Novel insights from a multiomics dissection of the Hayflick limit. Elife 10.7554/eLife.70283 (2022).
12. Munoz-Espin D & Serrano M Cellular senescence: from physiology to pathology. Nat. Rev. Mol. Cell Biol. 15, 482–496 (2014). [PubMed: 24954210]
13. Liu-Chittenden Y et al. Genetic and pharmacological disruption of the TEAD-YAP complex suppresses the oncogenic activity of YAP. Genes Dev. 26, 1300–1305 (2012). [PubMed: 22677547]
14. Anerillas C et al. A BDNF-TrkB autocrine loop enhances senescent cell viability. Nat. Commun. 13, 6228 (2022). [PubMed: 36266274]
15. Munk R et al. Acid ceramidase promotes senescent cell survival. Aging 13, 15750–15769 (2021). [PubMed: 34102611]
16. Stein C et al. YAP1 exerts its transcriptional control via TEAD-mediated activation of enhancers. PLoS Genet. 11, e1005465 (2015). [PubMed: 26295846]
17. Zanconato F et al. Genome-wide association between YAP/TAZ/TEAD and AP-1 at enhancers drives oncogenic growth. Nat. Cell Biol. 17, 1218–1227 (2015). [PubMed: 26258633]
18. Pakos-Zebrucka K et al. The integrated stress response. EMBO Rep 17, 1374–1395 (2016). [PubMed: 27629041]
19. Tabas I & Ron D Integrating the mechanisms of apoptosis induced by endoplasmic reticulum stress. Nat. Cell Biol. 13, 184–190 (2011). [PubMed: 21364565]
20. Anerillas C et al. Early SRC activation skews cell fate from apoptosis to senescence. Sci. Adv. 8, eabm0756 (2022). [PubMed: 35394839]
21. Hetz C & Papa FR The unfolded protein response and cell fate control. Mol. Cell 69, 169–181 (2018). [PubMed: 29107536]
22. Zhang D et al. A non-canonical cGAS-STING-PERK pathway facilitates the translational program critical for senescence and organ fibrosis. Nat. Cell Biol. 24, 766–782 (2022). [PubMed: 35501370]
23. Demaria M et al. Cellular senescence promotes adverse effects of chemotherapy and cancer relapse. Cancer Discov. 7, 165–176 (2017). [PubMed: 27979832]
24. Montalbano R et al. Endoplasmic reticulum stress plays a pivotal role in cell death mediated by the pan-deacetylase inhibitor panobinostat in human hepatocellular cancer cells. Transl. Oncol. 6, 143–157 (2013). [PubMed: 23544167]
25. Oslowski CM & Urano F Measuring ER stress and the unfolded protein response using mammalian tissue culture system. Methods Enzymol. 490, 71–92 (2011). [PubMed: 21266244]
26. Kim M, Kim T, Johnson RL & Lim DS Transcriptional co-repressor function of the hippo pathway transducers YAP and TAZ. Cell Rep. 11, 270–282 (2015). [PubMed: 25843714]
27. Tirado-Hurtado I, Fajardo W & Pinto JA DNA damage inducible transcript 4 gene: the switch of the metabolism as potential target in cancer. Front. Oncol. 8, 106 (2018). [PubMed: 29707520]
28. Lee Y et al. Histone deacetylase 4 reverses cellular senescence via DDIT4 in dermal fibroblasts. Aging 14, 4653–4672 (2022). [PubMed: 35680564]
29. Foltyn M et al. The physiological mTOR complex 1 inhibitor DDIT4 mediates therapy resistance in glioblastoma. Br. J. Cancer 120, 481–487 (2019). [PubMed: 30745581]
30. Herranz N et al. mTOR regulates MAPKAPK2 translation to control the senescence-associated secretory phenotype. Nat. Cell Biol. 17, 1205–1217 (2015). [PubMed: 26280535]

31. Laberge RM et al. MTOR regulates the pro-tumorigenic senescence-associated secretory phenotype by promoting IL1A translation. Nat. Cell Biol. 17, 1049–1061 (2015). [PubMed: 26147250]
32. Carroll B et al. Persistent mTORC1 signaling in cell senescence results from defects in amino acid and growth factor sensing. J. Cell Biol. 216, 1949–1957 (2017). [PubMed: 28566325]
33. Wu H et al. Integration of Hippo signalling and the unfolded protein response to restrain liver overgrowth and tumorigenesis. Nat. Commun. 6, 6239 (2015). [PubMed: 25695629]
34. Jacquemyn J, Cascalho A & Goodchild RE The ins and outs of endoplasmic reticulum-controlled lipid biosynthesis. EMBO Rep. 18, 1905–1921 (2017). [PubMed: 29074503]
35. Mossmann D, Park S & Hall MN mTOR signalling and cellular metabolism are mutual determinants in cancer. Nat. Rev. Cancer 18, 744–757 (2018). [PubMed: 30425336]
36. Brandt C et al. Food perception primes hepatic ER homeostasis via melanocortin-dependent control of mTOR activation. Cell 175, 1321–1335 (2018). [PubMed: 30445039]
37. Peterson TR et al. mTOR complex 1 regulates lipin 1 localization to control the SREBP pathway. Cell 146, 408–420 (2011). [PubMed: 21816276]
38. Quinn WJ 3rd et al. mTORC1 stimulates phosphatidylcholine synthesis to promote triglyceride secretion. J. Clin. Invest. 127, 4207–4215 (2017). [PubMed: 29035283]
39. Soto-Gamez A & Demaria M Therapeutic interventions for aging: the case of cellular senescence. Drug Discov. Today 22, 786–795 (2017). [PubMed: 28111332]
40. Birch J & Gil J Senescence and the SASP: many therapeutic avenues. Genes Dev. 34, 1565–1576 (2020). [PubMed: 33262144]
41. Freund A, Patil CK & Campisi J p38MAPK is a novel DNA damage response-independent regulator of the senescence-associated secretory phenotype. EMBO J. 30, 1536–1548 (2011). [PubMed: 21399611]
42. Dorr JR et al. Synthetic lethal metabolic targeting of cellular senescence in cancer therapy. Nature 501, 421–425 (2013). [PubMed: 23945590]
43. Ovadya Y et al. Impaired immune surveillance accelerates accumulation of senescent cells and aging. Nat. Commun. 9, 5435 (2018). [PubMed: 30575733]
44. Schafer MJ et al. Cellular senescence mediates fibrotic pulmonary disease. Nat. Commun. 8, 14532 (2017). [PubMed: 28230051]
45. Angelidis I et al. An atlas of the aging lung mapped by single cell transcriptomics and deep tissue proteomics. Nat. Commun. 10, 963 (2019). [PubMed: 30814501]
46. Tabula Muris C A single-cell transcriptomic atlas characterizes ageing tissues in the mouse. Nature 583, 590–595 (2020). [PubMed: 32669714]
47. Goplen NP et al. Tissue-resident $CD8^+$ T cells drive age-associated chronic lung sequelae after viral pneumonia. Sci. Immunol. 10.1126/sciimmunol.abc4557 (2020).
48. Schneider JL et al. The aging lung: physiology, disease, and immunity. Cell 184, 1990–2019 (2021). [PubMed: 33811810]
49. Gillich A et al. Capillary cell-type specialization in the alveolus. Nature 586, 785–789 (2020). [PubMed: 33057196]
50. Wolf T et al. Dynamics in protein translation sustaining T cell preparedness. Nat. Immunol. 21, 927–937 (2020). [PubMed: 32632289]
51. Prata L, Ovsyannikova IG, Tchkonia T & Kirkland JL Senescent cell clearance by the immune system: emerging therapeutic opportunities. Semin. Immunol. 40, 101275 (2018). [PubMed: 31088710]
52. Desdin-Mico G et al. T cells with dysfunctional mitochondria induce multimorbidity and premature senescence. Science 368, 1371–1376 (2020). [PubMed: 32439659]
53. Kale A, Sharma A, Stolzing A, Desprez PY & Campisi J Role of immune cells in the removal of deleterious senescent cells. Immun Ageing 17, 16 (2020). [PubMed: 32518575]
54. Marin I, Serrano M & Pietrocola F Recent insights into the crosstalk between senescent cells and CD8 T lymphocytes. NPJ Aging 9, 8 (2023). [PubMed: 37015935]
55. Lopez-Otin C, Blasco MA, Partridge L, Serrano M & Kroemer G Hallmarks of aging: an expanding universe. Cell 186, 243–278 (2023). [PubMed: 36599349]

56. Ogrodnik M et al. Cellular senescence drives age-dependent hepatic steatosis. Nat. Commun. 8, 15691 (2017). [PubMed: 28608850]
57. Mylonas KJ et al. Cellular senescence inhibits renal regeneration after injury in mice, with senolytic treatment promoting repair. Sci. Transl. Med. 10.1126/scitranslmed.abb0203 (2021).
58. Yang J et al. Guidelines and definitions for research on epithelial-mesenchymal transition. Nat. Rev. Mol. Cell Biol. 21, 341–352 (2020). [PubMed: 32300252]
59. Anerillas C, Altes G & Gorospe M MAPKs in the early steps of senescence implemEMTation. Front. Cell Dev. Biol. 11, 1083401 (2023). [PubMed: 37009481]
60. Chen H et al. MacroH2A1 and ATM play opposing roles in paracrine senescence and the senescence-associated secretory phenotype. Mol. Cell 59, 719–731 (2015). [PubMed: 26300260]
61. Hernandez-Segura A, Nehme J & Demaria M Hallmarks of cellular senescence. Trends Cell Biol. 28, 436–453 (2018). [PubMed: 29477613]
62. Wang M et al. Verteporfin is a promising anti-tumor agent for cervical carcinoma by targeting endoplasmic reticulum stress pathway. Front. Oncol. 10, 1781 (2020). [PubMed: 33014875]
63. Salama R, Sadaie M, Hoare M & Narita M Cellular senescence and its effector programs. Genes Dev. 28, 99–114 (2014). [PubMed: 24449267]
64. Narita M et al. Spatial coupling of mTOR and autophagy augments secretory phenotypes. Science 332, 966–970 (2011). [PubMed: 21512002]
65. Moya IM & Halder G Hippo-YAP/TAZ signalling in organ regeneration and regenerative medicine. Nat. Rev. Mol. Cell Biol. 20, 211–226 (2019). [PubMed: 30546055]
66. Strano S et al. The transcriptional coactivator Yes-associated protein drives p73 gene-target specificity in response to DNA Damage. Mol. Cell 18, 447–459 (2005). [PubMed: 15893728]
67. Furth N, Aylon Y & Oren M p53 shades of Hippo. Cell Death Differ. 25, 81–92 (2018). [PubMed: 28984872]
68. Sladitschek-Martens HL et al. YAP/TAZ activity in stromal cells prevents ageing by controlling cGAS-STING. Nature 607, 790–798 (2022). [PubMed: 35768505]
69. Sturmlechner I et al. Senescent cells limit p53 activity via multiple mechanisms to remain viable. Nat. Commun. 13, 3722 (2022). [PubMed: 35764649]
70. van Deursen JM Senolytic therapies for healthy longevity. Science 364, 636–637 (2019). [PubMed: 31097655]
71. Xu M et al. Senolytics improve physical function and increase lifespan in old age. Nat. Med. 24, 1246–1256 (2018). [PubMed: 29988130]
72. Wang B et al. An inducible p21-Cre mouse model to monitor and manipulate p21-highly-expressing senescent cells in vivo. Nat Aging 1, 962–973 (2021). [PubMed: 35024619]
73. Chaib S, Tchkonia T & Kirkland JL Cellular senescence and senolytics: the path to the clinic. Nat. Med. 28, 1556–1568 (2022). [PubMed: 35953721]
74. Yosef R et al. Directed elimination of senescent cells by inhibition of BCL-W and BCL-XL. Nat. Commun. 7, 11190 (2016). [PubMed: 27048913]
75. Love MI, Huber W & Anders S Moderated estimation of fold change and dispersion for RNA-seq data with DESeq2. Genome Biol 15, 550 (2014). [PubMed: 25516281]
76. Kuleshov MV et al. Enrichr: a comprehensive gene-set enrichment analysis web server 2016 update. Nucleic Acids Res. 44, W90–W97 (2016). [PubMed: 27141961]
77. Subramanian A et al. Gene-set enrichment analysis: a knowledge-based approach for interpreting genome-wide expression profiles. Proc. Natl Acad. Sci. USA 102, 15545–15550 (2005). [PubMed: 16199517]
78. Roopra A MAGIC: A tool for predicting transcription factors and cofactors driving gene sets using ENCODE data. PLoS Comput. Biol. 16, e1007800 (2020). [PubMed: 32251445]

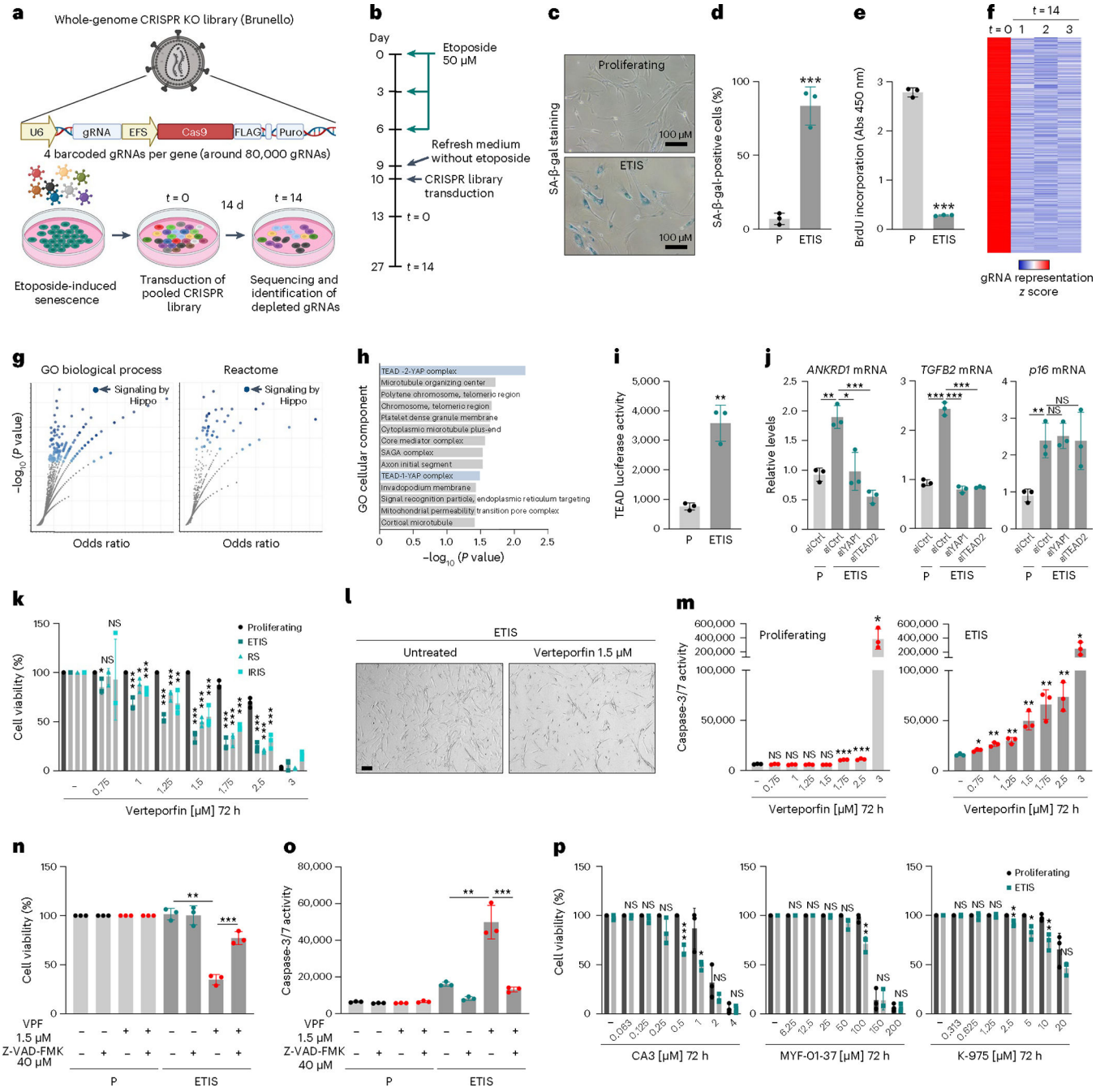

Fig. 1 |. CRISPR screen identifies YAP–TEAD pathway as essential for senescent cell viability.

a,**b**, CRISPR screen performed on ETIS WI-38 fibroblasts (**a**), including timeline of treatments and procedures (**b**). **c**,**d**, Representative images of SA-β-gal staining (**c**) and quantification (**d**) in proliferating (P) and ETIS WI-38 cells. Scale bar, 100 μm. **e**, BrdU assay performed in the conditions described in **c**. Abs, absorbance. **f**, Heat map representation of *z* scores of gRNAs significantly reduced when comparing $t = 14$ to $t = 0$ (Supplementary Table 1). **g**, Analysis of gRNAs depleted from the $t = 14$ experimental groups (Methods) with Enrichr (Supplementary Table 2). Dot plots show the combined score

(*y* and *x* axes) of 'Signaling by Hippo' categories from GO and Reactome databases. For each category (dots present in the plot), the *y* axis represents $-\log_{10}$(*P* value) and the *x* axis represents odds ratios. **h**, Bar plot showing combined scores of GO database 'Cellular component' obtained by Enrichr analysis of the conditions described in **g**. **i**, Luciferase activity of a TEAD reporter construct analyzed for the indicated experimental groups. **j**, RT–qPCR analysis of the indicated mRNAs in ETIS WI-38 cells transfected with siCtrl, siYAP1 or siTEAD2; 24 h later, cells were treated with etoposide (50 μM, 8 d). Proliferating cells transfected with siCtrl were included as controls. **k**, Cell viability analysis by direct cell counting after treating with the indicated VPF doses (72-h treatments). WI-38 fibroblasts were proliferating or rendered senescent by ETIS, RS or IRIS. **l**, Representative micrographs of ETIS WI-38 cells that were either untreated or treated with VPF (1.5 μM, 72 h). Scale bar, 100 μm. **m**, Caspase-3/caspase-7 activity measurement in either proliferating or ETIS WI-38 cells treated with the indicated doses of VPF for 72 h. **n**,**o**, Cell viability evaluation by direct cell counting (**n**) and caspase-3/7 activity measurement (**o**) in proliferating and ETIS WI-38 cells treated with VPF for 72 h; apoptosis was rescued by simultaneous treatment with Z-VAD-FMK where indicated. **p**, Cell viability analysis by direct cell counting of either proliferating or ETIS WI-38 cells with the indicated doses of YAP–TEAD inhibitors for 72 h. Graphs in **d**, **e**, **i**–**k** and **m**–**p** display the means and each individual value as a dot ± s.d. of $n = 3$ independent replicates; significance (*$P < 0.05$, **$P < 0.01$, ***$P < 0.001$) was determined using two-tailed Student's *t*-test. Unless indicated, statistical tests were performed relative to untreated or proliferating controls. See also Extended Data Fig. 1. NS, not significant.

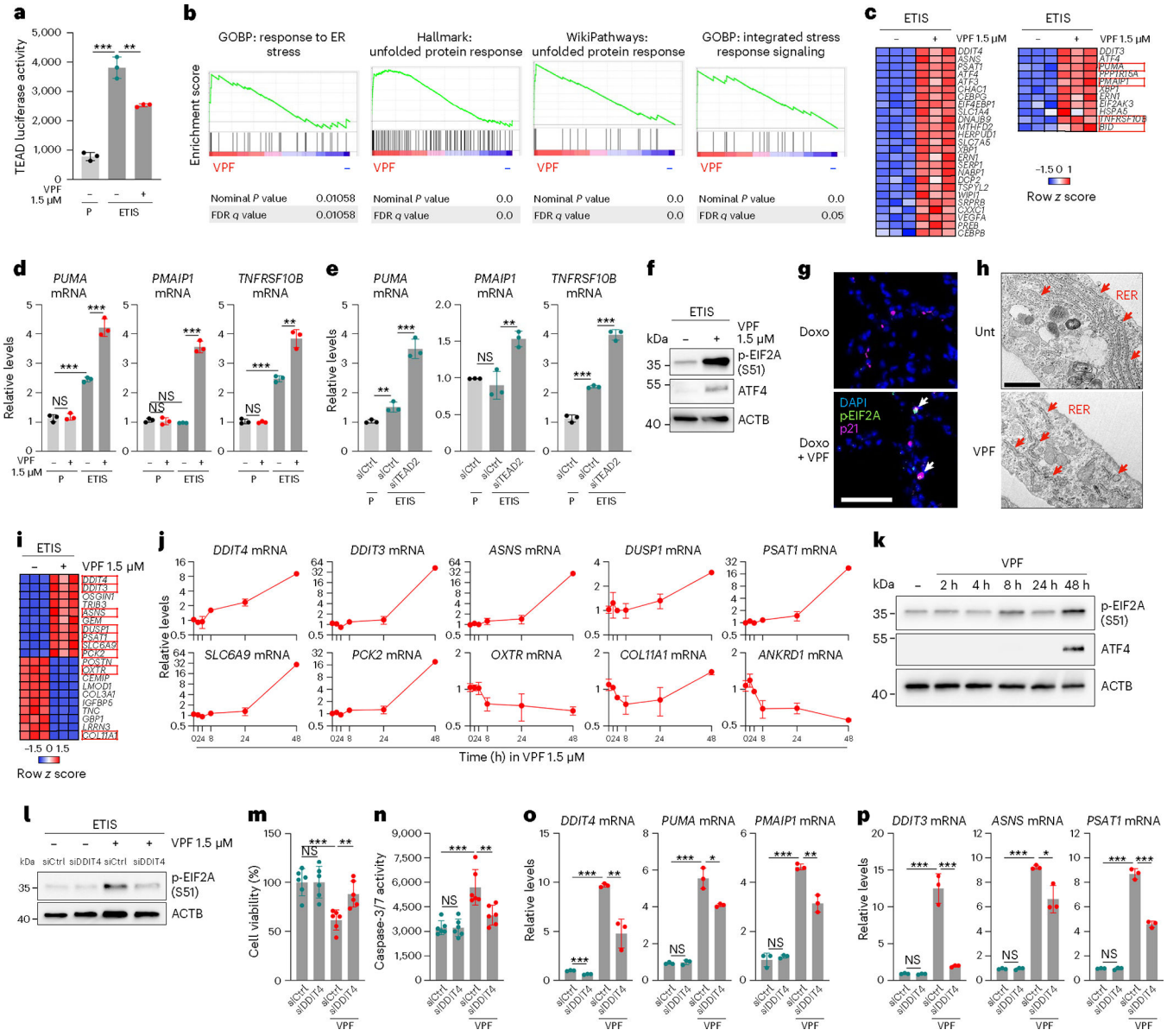

Fig. 2 |. YAP–TEAD inhibition triggers apoptosis by derepressing DDIT4, causing endoplasmic reticulum stress.

a,**b**, Luciferase activity from the TEAD promoter as measured in ETIS WI-38 cells treated with VPF (1.5 μM, 48 h) or untreated; control proliferating (P) cells (**a**) and GSEA of RNA-seq data from ETIS WI-38 cells (VPF relative to control untreated) (**b**). Shown are transcriptomes associated with VPF-treated versus untreated ETIS WI-38 cells; FDR, false discovery rate; GOBP, GO Biological Process. **c**, Heat map displaying the levels of each transcript in the GSEA gene sets shown in **b** (Hallmark: UPR, left; WikiPathways: UPR, right). Red boxes indicate mRNAs encoding pro-apoptotic proteins. **d**, RT–qPCR analysis of the indicated transcripts in P and ETIS WI-38 cells treated as in **a**. **e**, RT–qPCR quantification of the indicated transcripts in ETIS WI-38 cells transfected with siCtrl or siTEAD2 1 d before inducing senescence. Proliferating WI-38 cells transfected with siCtrl were included as controls. **f**, Representative western blot analysis ($n = 3$ independent

experiments) of the indicated proteins in WI-38 cells treated as in **b**. **g**, Representative immunofluorescence micrographs from lungs of mice ($n = 6$) that were injected with doxorubicin 10 d earlier, then treated daily for 4 d with either DMSO or VPF (50 mg per kg body weight) from day 6 onward (Extended Data Fig. 4a). Cells were stained to visualize nuclei (DAPI, blue), phosphorylated EIF2A (S51; green) and p21 (purple); white arrows point to double-stained cells. Scale bar, 50 μm. **h**, Representative images of TEM of ETIS WI-38 cells treated with VPF as in **a**, along with untreated controls (Unt). Red arrows point to rough endoplasmic reticulum (RER). Scale bar, 1 μm. **i**, Heat map displaying the row z score of each of the transcripts indicated (top 10 increased and decreased in VPF-treated versus untreated ETIS WI-38 cells) between conditions. Red boxes denote mRNAs transcriptionally regulated by YAP–TEAD complex and involved in the ER stress response. **j**, RT–qPCR analysis of YAP–TEAD target mRNAs at the indicated times after treating ETIS WI-38 cells with 1.5 μM VPF. **k**, Western blot analysis ($n = 3$) of the indicated proteins in cells treated as in **j**. **l**, Western blot analysis ($n = 3$) of the indicated proteins in ETIS WI-38 cells transfected with the indicated short interfering RNAs (siRNAs), then treated or not with VPF (1.5 μM, 48 h). **m**,**n**, Cell viability assessments by direct cell counting (**m**) and caspase-3/caspase-7 activity (**n**) for the groups in **l**, although treated for 72 h instead. **o**,**p**, RT–qPCR analysis of mRNAs in the experimental groups in **l**. Graphs in **a**, **d**,**e**,**j**,**o** and **p** show each individual value as a dot and the means ± s.d. of $n = 3$ independent replicates; graphs in **m** and **n** show each individual value as a dot and the means ± s.d. of $n = 6$ independent replicates; significance (*$P < 0.05$, **$P < 0.01$, ***$P < 0.001$) was calculated by performing two-tailed Student's t-test. See also Extended Data Fig. 2.

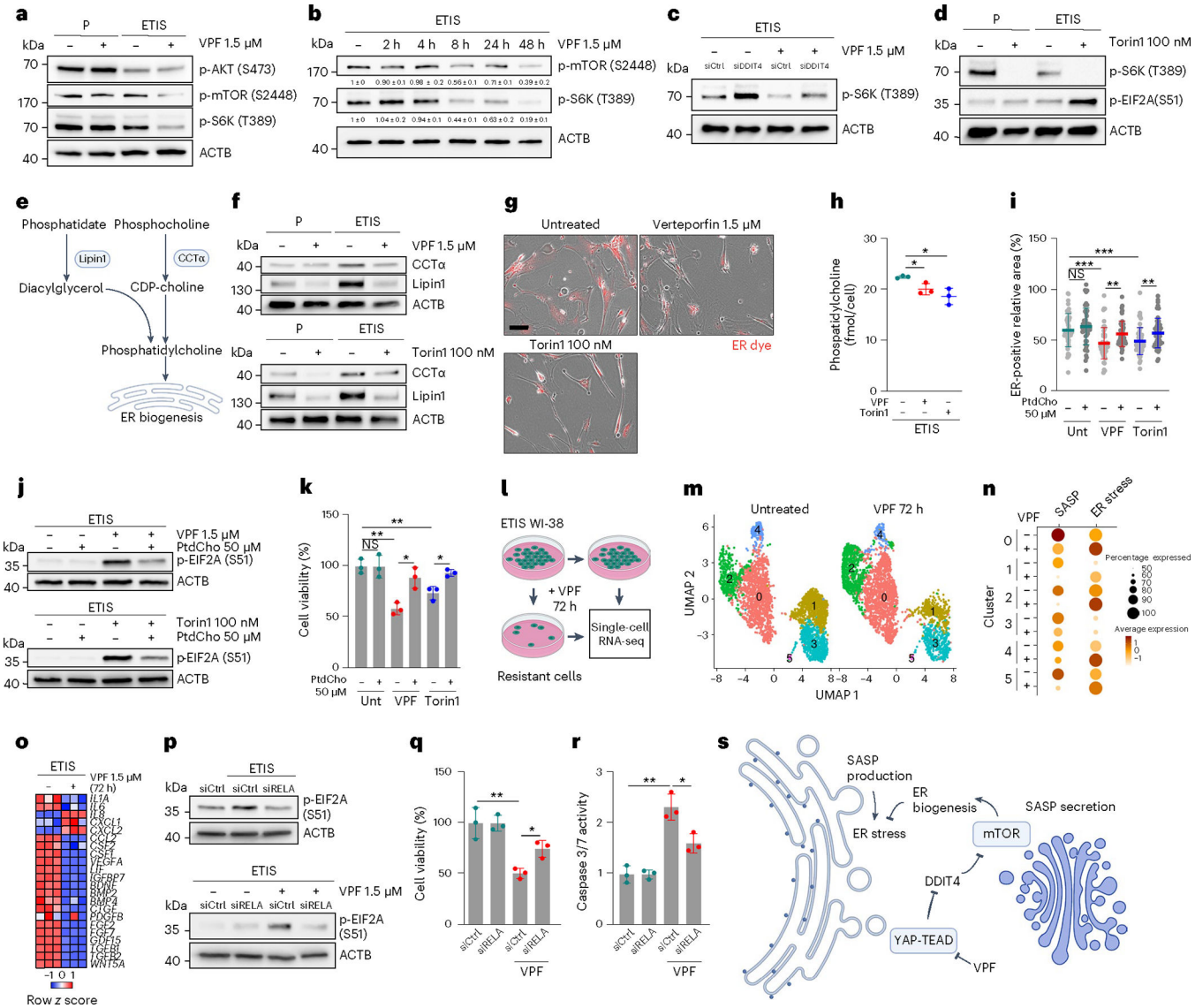

Fig. 3 |. Inhibition of mTOR-dependent endoplasmic reticulum biogenesis by DDIT4 induces endoplasmic reticulum stress and senolysis.

a, Western blot analysis ($n = 3$) of the indicated proteins in proliferating (P) or ETIS WI-38 cells, treated or not with VPF (1.5 μM, 48 h), starting at day 6 of etoposide treatment. **b**, Western blot analysis ($n = 3$) of the indicated proteins at different times after treatment with 1.5 μM VPF. Normalized phosphorylation values (p-mTOR or p-p70 S6K/ACTB) below each lane were calculated (means ± s.d.) relative to untreated controls. **c**, Western blot analysis ($n = 3$) of the indicated proteins in ETIS WI-38 cells transfected with siCtrl or siDDIT4 and treated with VPF (1.5 μM, 48 h) or not. **d**, Western blot analysis ($n = 3$) of the indicated proteins in P and ETIS WI-38 cells 48 h after treatment with Torin1 (100 nM) or no treatment. **e**, Schematic depicting mTOR-regulated enzymes lipin-1 and CCTα, regulators of PtdCho biosynthesis and ER biogenesis. **f**, Western blot analysis ($n = 3$) of the specified proteins after treatment of P or ETIS WI-38 cells, with 1.5 μM VPF or 100 nM Torin1 for 48 h, as in **a** and **d**. **g**, Micrographs depicting the relative ER area stained

with ER tracker (red) in ETIS WI-38 cells that were either untreated or treated with 1.5 μM VPF or 100 nM Torin1 for 48 h. Scale bar, 100 μm. **h**, Dot plot representation of the levels of PtdCho (fmol per cell) as measured in the conditions described in **g**. **i**, Dot plot representation of ER-positive areas per cell for the experimental groups in **g**; each treatment was simultaneously supplemented with 50 μM PtdCho. **j**, Western blot analysis ($n = 3$) of the specified proteins with the indicated treatments performed for 48 h in ETIS WI-38 cells. **k**, Cell viability assessment by direct cell counting for the groups in **i**, although treated for 72 h. **l**,**m**, Experimental scheme to identify single-cell transcriptomic differences between ETIS WI-38 that were untreated or treated with VPF (1.5 μM, 72 h) to eliminate those cells most sensitive to VPF (**l**), and uniform manifold approximation and projection (UMAP) identification of six subgroups in ETIS WI-38 cells and ETIS WI-38 cells treated with VPF (1.5 μM, 72 h; **m**). **n**, Dot plot showing the association of transcriptome clusters described in **m** with ER stress (GOBP: response to ER stress), apoptosis (Hallmark: apoptosis) and SASP (custom gene set, 132 markers). Dot size, proportion of cells expressing transcripts in a gene set; dot color, scaled expression level. **o**, Heat map, levels of mRNAs for the conditions described in **l**. **p**, Western blot analysis ($n = 3$) of the indicated proteins in proliferating and ETIS WI-38 cells with the combinations of siRNAs and VPF (1.5 μM, 48 h) shown. siCtrl-transfected, proliferating controls were included. **q**,**r**, Cell viability assessment by direct cell counting (**q**) and caspase-3/caspase-7 activity measurement (**r**) in ETIS WI-38 cells for 72 h in the presence of the indicated siRNAs and VPF. **s**, Proposed model for YAP–TEAD support of senescent cell viability; see the main text for details. Graphs in **h**,**i**,**k**,**q** and **r** show each individual value as a dot and the means ± s.d. of $n = 3$ independent replicates; the graph in **i** shows individual values of 20 different cells from 3 independent replicates (total 60 individual values); significance (*$P < 0.05$, **$P < 0.01$, ***$P < 0.001$) was calculated using a two-tailed Student's *t*-test. See also Extended Data Fig. 3.

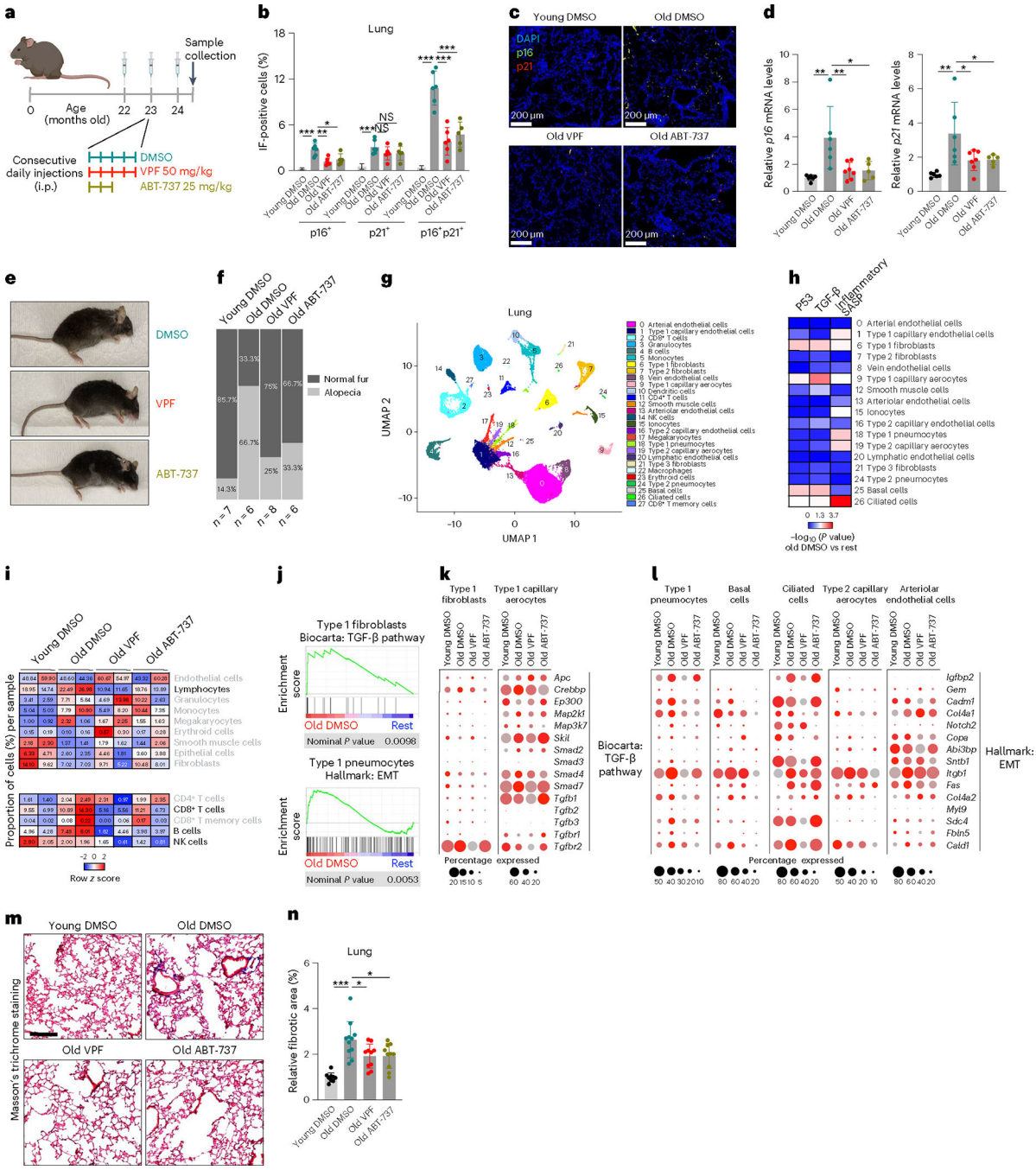

Fig. 4 |. VPF treatment reduces senescent cell burden in vivo.

a, Treatment regimens followed for each experimental group in this study (DMSO, 50 mg per kg body weight VPF and 25 mg per kg body weight ABT-737) in naturally aged mice. Young mice (3 months old) treated with one round of DMSO were included as controls. i.p., intraperitoneal. **b**,**c**, Quantification of percentages (**b**) and representative micrographs (**c**) of p16-positive, p21-positive or p16/p21 double-positive cells in lungs of the groups described in **a**. **d**, RT–qPCR analysis of the levels of *p16* and *p21* mRNAs (normalized to *Actb* mRNA) in lungs of mice described in **a**. **e**, Appearance of representative mice at

the end of the study in the groups described in **a**. **f**, Quantification of alopecia incidence in the indicated groups. **g**, UMAP clustering of cells identified by scRNA-seq performed in lung samples from each of the conditions described in **a**. UMAP plots display all eight samples together; each sample alone can be viewed (Extended Data Fig. 5b). **h**, Heat map indicating the association score ($-\log_{10}(P \text{ value})$) of p53, TGF-β and inflammatory SASP transcriptomic signatures for the cell types identified in **g**, excluding hematopoietic clusters. **i**, Heat maps represent row *z* score and proportions of different cell types (percentage from total; op heat map) and lymphoid cell clusters (bottom heat map) identified by scRNA-seq analysis. **j**, GSEA association of the indicated cell types from 'old DMSO' (compared to the rest of the experimental groups) with the indicated gene sets (Biocarta: TGF-β pathway; Hallmark: ENT). **k**,**l**, Dot plot representations of associations between cell types and conditions with the top 15 transcripts from either Biocarta: TGF-β pathway (**k**) or Hallmark: EMT (**l**). Dot sizes represent percentages of cells expressing a transcript, while intensities of red indicate relative expression values. **m**,**n**, MTC staining of lung samples from **c**, with representative MTC staining (**m**) in blue and quantification of blue areas in each sample divided by total area in red (**n**). Scale bar, 200 μm. Data in **b**,**d** and **n** represent individual values as dots and the means ± s.d. of the mice studied (Supplementary Table 6); significance ($*P < 0.05$, $**P < 0.01$, $***P < 0.001$) was calculated using one-way analysis of variance. See also Extended Data Figs. 4 and 5.